Comptes Rendus

Chimie

Alice Am, Laura Trapiella-Alfonso, Camille Lescot, Bich-Thuy Doan,
Fanny d'Orlyé and Anne Varenne

From design to formulation of peptide building blocks for nanotheranostic applications: a synergistic multidisciplinary investigation

Account

From design to formulation of peptide building blocks for nanotheranostic applications: a synergistic multidisciplinary investigation

Alice Am [a], **Laura Trapiella-Alfonso** [a], **Camille Lescot** [a], **Bich-Thuy Doan** [a], **Fanny d'Orlyé** [a] and **Anne Varenne** [*, a]

[a] Institute of Chemistry for Life & Health Sciences (iCLeHS), Chimie ParisTech, PSL University, CNRS 8060, 75005, Paris, France

E-mail: anne.varenne@chimieparistech.psl.eu (A. Varenne)

Abstract. This study presents the journey of a collaborative project for the development of biocompatible nanotheranostic tools, based on peptide self-assembling nanostructures. The peptide sequences were designed to combine smart drug delivery and imaging properties. For this purpose, the selected sequences present: (1) an amphiphilic character for self-assembling properties, efficient hydrophobic drugs encapsulation and efficient biodistribution; (2) a pH-sensitive self-assembly for drug delivery under pH modification in the environment of cancer cells; (3) a receptor-targeting motif within the peptide sequence, overexpressed by certain cancer cells, for specific and controlled delivery of the active ingredient to tumors; (4) accessible functions for further functionalization with a contrast agent for diagnosis. These sequences were first synthesized in a continuous flow to provide a rapid and versatile synthetic process, while lowering reactant consumption, and the synthetic route was optimized through the development of an electrokinetic method coupled to UV–visible detection (CE-UV) and mass spectrometry (CE-MS) that allowed a powerful physicochemical characterization in terms of sequence identification and purity. Few pertinent peptide sequences were then functionalized with a complex of gadolinium to generate Magnetic Resonance Imaging (MRI) properties, and this functionalization step was also optimized and controlled by CE-MS. The formulation procedure was then developed by a deep physicochemical characterization of the peptide nanostructures and the combination of analytical and physical methods to highlight the mechanisms generating the quick reversible self-assembly. Finally, MRI imaging studies on both monomers and nanostructures evidenced a good MRI contrast with properties adapted for a short half-life time.

Keywords. Short synthetic amphiphilic peptides, Continuous flow SPPS peptide synthesis aided by CE-MS, Peptide self-assembly, Physicochemical characterization, MRI, Theranostic agents.

1. Introduction

Currently, the treatment of most diseases uses drugs, in the form of formulation of active pharmaceutical ingredients. However, their therapeutic effect is often significantly reduced due to low bioavailability, linked to poor pharmacokinetics generated by low chemical stability, solubility, or even too rapid metabolism leading to premature elimination of the drug, therefore requiring several doses [1,2]. Furthermore, the absence of targeting specific areas (tumors, inflammatory sites, etc.) leads to random drug delivery, which can cause significant

---

*Corresponding author

side effects and result in poor patient treatment tolerance.

For more than three decades, numerous nanomaterials have been developed as drug delivery systems. Such nanovectors can combine several functionalities and physicochemical properties to improve pharmacokinetics compared to the non-encapsulated drug [3]. Among these functionalities, the integration of imaging probes is of significance in designing theranostic nanoobjects, providing simultaneous therapeutic properties and monitoring for image-guided therapy. Thus, the biodistribution of the nanovector can be studied in a non-invasive manner [4]. Furthermore, the addition of specific targeting ligands on the nanoobject enable the detection of diseases at an early stage and would increase the chance of recovery thanks to early diagnosis [5]. This specific targeting is also relevant for targeted delivery of anticancer drugs into tumors, since these active molecules are generally cytotoxic, thus limiting toxicity to healthy cells.

Despite the development of numerous theranostic nanoobjects, their translation into clinical practice remains difficult due to concerns about the safety of these products. Indeed, the elimination of nanoparticles in the body strongly depends on their physicochemical properties, i.e., size, shape, surface charge, and the nature of the material [6]. Thus, there is a growing interest in biodegradable and biocompatible nanomaterials, formed from natural building blocks, such as nanostructures based on peptide self-assembly [7]. Peptides are versatile biopolymers which present a great diversity of sequences, including sequences capable of self-assembling into nanoarchitectures of various structures. The peptide sequence can be controlled during the synthesis and the presence of reactive chemical functions on the peptide facilitates its functionalization with targeting ligands, imaging probes or therapeutic molecules [8]. Peptide self-assemblies can also lead to intelligent nanoobjects sensitive to endogenous or exogenous stimuli. For example, pH variations in the body are often associated with pathologies, such as cancer. Thus, peptides could be designed to self-assemble reversibly depending on the pH [9]. For delivery of anticancer drugs, the disassembly of the nanostructure in response to a variation of pH would trigger the release of the active molecule. Specific nanostructures based on peptide self-assembly were developed for the targeted delivery of anticancer drugs, thanks to peptides specifically targeting receptors overexpressed by certain tumors, and controlled by an endogenous stimulus, including pH as well as the presence of reactive oxygen species or enzymatic activity [10]. Contrast agents based on peptide self-assembly are also described, particularly for Magnetic Resonance Imaging (MRI), with better performances than molecular MRI probes [11]. Nanoobjects have already been studied for drug delivery [12] or as imaging probes [13], but a combination of the two characteristics is still in its infancy.

Few nanotheranostic agents based on self-assembled peptides were designed to be used simultaneously as a drug carrier and an imaging probe. In these use cases, the peptide sequences contain an RGD (R = Arg; G = Gly; D = Asp) or an octreotide motif to target the $\alpha v \beta 3$ integrin somatostatin receptors, respectively, overexpressed by tumor cells in certain types of cancers [14,15]. An MRI probe was also conjugated to the peptide for in vivo tracking of nanoobjects, with the aim of improving the contrast of images generated in MRI. However, the nanoobjects described in these examples are not stimuli-responsive and the delivery of drugs is carried out by sustained release.

Therefore, challenges persist in the design of nanotheranostic tools capable of actively targeting certain areas. First, sensitivity of the nanoobject to an endogenous stimulus is essential for real control of drug delivery in the targeted area. Thus, the disassembly of the structure under a stimulus would trigger the release of the active ingredient and the peptides serving as building blocks will be quickly eliminated. Furthermore, the integration of the MRI probe into the nanoobject must be done in a way that does not interfere with the peptide self-assembly and the interaction between the targeting ligand and its receptor, while maintaining the imaging properties of the probe.

The development of self-assembled nanoobjects providing all the aforementioned properties relies heavily on the design of the peptide sequence serving as the basic block. Among the different peptide sequences having self-assembly properties, amphiphilic peptides were selected as they can form micelle-type structures, suitable for the encapsulation of hydrophobic therapeutic molecules [16]. These amphiphilic sequences should be further

designed for smart drug delivery, coupling both a targeting motif to a receptor and a region that is sensitive to an endogenous stimulus, as well as for functionalization with a MRI probe. As batch peptide synthesis is time-consuming, its transfer to a continuous flow process would help to reduce total synthesis time and simplify handling [17]. A structural characterization and purity of synthesized crude peptides is important for their further use as building blocks for self-assembly. Although it is generally carried out using conventional methods such as Nuclear Magnetic Resonance (NMR) and Mass Spectrometry (MS), these methods are not sufficient for the analysis of peptide mixtures.

In this study, we established a strategy to develop these new self-assembled amphiphilic peptide building blocks by combining areas of expertise in synthesis, analytical methods, physicochemical characterizations and MRI studies. The design of the peptide sequences, the optimization of their synthesis, and the deep mechanistic understanding and optimization of their self-assembly process, were facilitated by various methods, notably CE-MS and MRI. This deep characterization and understanding of the self-assembly mechanisms lays the groundwork for development of novel and efficient theranostic agents, and may limit animal testing.

2. Strategy for the design of amphiphilic peptide building blocks for nanotheranostic applications

As a starting point, the peptide sequence VVVVVVKKGRGDS (P1), described by Liang et al. was chosen [18]. This amphiphilic sequence consists of a hydrophobic tail with six valines (V = Val), which can form hydrophobic interactions and promote peptide self-assembly. The sequence also contains an RGD (R = Arg; G = Gly; D = Asp) motif for targeting αvβ3 integrins, overexpressed at the surface of cancer cells. After self-assembly of the peptide, these RGDs are exposed at the nanostructure surface and available to interact specifically with these receptors and promote internalization of the nanoobject into cancer cells. The presence of two lysines (K = Lys) confers a pH-dependent character to the sequence, so that at pH 5, the ratio of protonated lysine to deprotonated lysine is 100 times greater than at pH 7, preventing self-assembly at acidic pH due to

electrostatic repulsion. In tumor tissue, the environment is slightly acidic, with a pH close to 6.8, but decreases further in intracellular endosomes where the pH is 4.5 [19]. A pH-dependent self-assembly is then conducive for the triggered release of antitumor drugs in tumors, by decrease in the pH (Figure 1).

To advance the design of a nanotheranostic agent, an imaging probe is functionalized onto the peptide sequence. The peptide P1 provides various amine and carboxylic groups, located on the sequence. The functionalization of the amines would lead to insertion of the probe inside the nanostructure, thus modifying the self-assembly process and the probe properties. On the other hand, the functionalization of the terminal carboxylic acid or the side chain of aspartic acid (D = Asp) through amide bond formation, could lead to possible side reactions such as peptide polycondensation. Temporary protection of these groups could be performed, but is a multi-step functionalization process. Therefore, a new amphiphilic peptide sequence was designed by incorporating a cysteine (C = Cys) into P1, introducing a thiol group positioned in the hydrophilic head to produce P2. This modification allows for easy participation in a click chemical reaction. As the aim is to develop MRI contrast agents, a complexation with [(2-(4,7,10-tris(carboxymethyl)-1,4,7,10-tetraazacyclododecan-1-yl) pentanedioic acid)] maleimide (DOTAGA-maleimide) was explored by a thiol-maleimide conjugation, followed by a gadolinium complexation step, as DOTAGA is a classical complexing agent for gadolinium.

The development of this new optimized sequence VVVVVVKKGRGDCS (P2) offers the following advantages: (1) a biocompatible and biodegradable sequence, purely composed of natural amino acids; (2) its potential self-assembly in an aqueous medium, allowing encapsulation of hydrophobic drugs; (3) the presence of the RGD motif specifically targeting αvβ3 integrin receptors, overexpressed at the surface of cancer cells, allowing targeted drug delivery; (4) the pH dependence of self-assembly leading to disassembly of the nanoobject at pH less than 5, allowing drug release triggered by a pH decrease in tumor microenvironments. These characteristics enable peptide self-assembly to constitute an intelligent nanovector for targeted and controlled delivery of anticancer drugs. To complete the properties for theranostic applications, the Gd(DOTAGA)
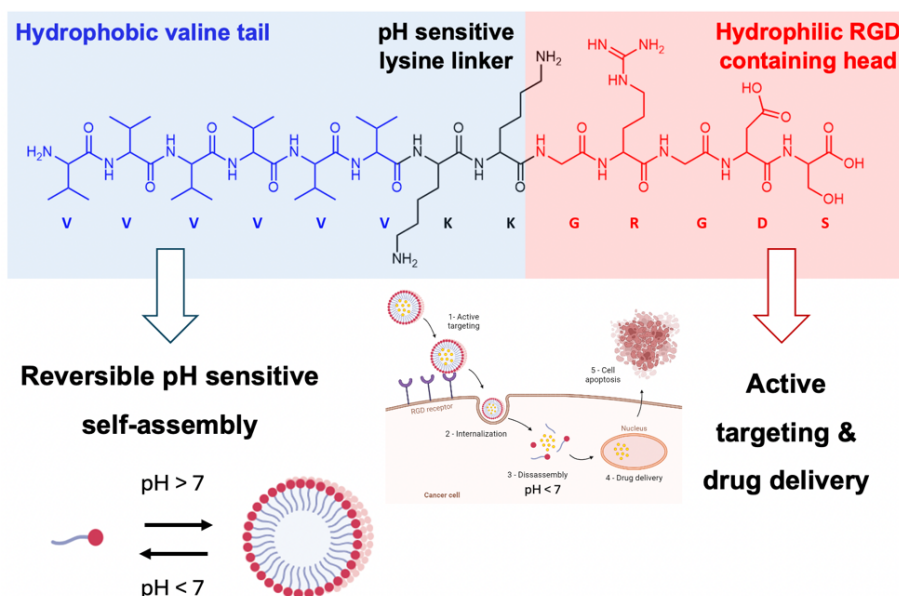
Figure 1. Amphiphilic peptide sequence VVVVVVKKGRGDS (P1), presenting a reversible pH-sensitive self-assembly and properties for the targeted release of anti-cancer molecules into tumor cells. Adapted from Ref. [18].

modified peptide sequence should preserve the self-assembling properties while providing imaging properties to the nanoobject, allowing it to be monitored in vivo.

Thus, in a first step, the synthesis process was developed by solid-phase peptide synthesis, using a continuous flow process. The synthesis products were first analyzed using classical characterization methods, NMR and MS. As they are time-consuming and present limitations for complex mixtures, a separation step prior to detection was evidenced as mandatory. An electrokinetic method coupled to mass spectrometry via an ionization–desorption interface by electro nebulization (CE-ESI-MS) was simultaneously developed to quickly assess the structure and purity of synthesized crude peptides, aiding in the optimization of peptide synthesis. Indeed, CE-ESI-MS is a robust analytical method combining the resolving power of capillary electrophoresis (CE) and the sensitivity of MS, which allows a more detailed characterization of synthetic peptides [20]. Further functionalization by click chemistry with a Gd(DOTAGA) was then developed to generate an MRI probe. CE-ESI-MS was also used to monitor the progress of the reaction and study the

continuous stability of the conjugated products. Finally, an in-depth study of the self-assembly process of all the synthesized peptide building blocks was carried out using several complementary physicochemical characterization methods, such as Dynamic Light Scattering (DLS), Transmission Electron Microscopy (TEM), Circular Dichroism (CD), zetametry, Taylor Dispersion Analysis (TDA) and CE-UV. Co-assemblies of functionalized and non-functionalized peptides were then studied to better understand the formulation process, and their magnetic relaxivities were measured by MRI methods. The deep physicochemical characterization of self-assembled or co-assembled nanoobjects are important in predicting their pharmacokinetics.

3. Efficient synthesis of peptide building blocks by continuous flow guided by electrophoretic separation coupled to mass spectrometry detection

The development of nanovectors based on self-assembling peptides relies first and foremost on the design and the synthesis of the peptide building blocks. Therefore, a versatile synthesis process was

developed, that could be optimized by physicochemical characterization of the reaction products using CE-ESI-MS.

The development and large-scale production of therapeutic peptides by Solid-Phase Peptide Synthesis (SPPS) is the method of choice for peptide synthesis. As a result, due to the continuous need to develop new reagents, resins, linkers, protected amino acids, etc., there is now a wide choice of commercial products at relatively affordable costs to synthesize almost any type of peptides. Similarly, at laboratory scale, specific reactors have been developed for manual SPPS (volume greater than 10 mL), called "batch" synthesis, as well as microwave-assisted synthesizers for automated synthesis adapted for SPPS with the 9-fluorenylmethoxycarbonyl (Fmoc) strategy [21]. Microwave-assisted synthesis remains the method of choice for the construction of long or difficult sequences. Nevertheless, over the last decade, there has been renewed interest in continuous flow peptide synthesis, which offers significant advantages over the above-mentioned processes [17]. Continuous flow SPPS is performed by the loading of a resin containing grafting sites (alcohol functions in this study) into a fixed-bed reactor, through which the reagents and solvents are percolated [21]. The immobilization of the resin in the reactor permits: (1) reducing the required amount of solvent and reactant amounts and the total synthesis time [22]; (2) generating an efficient and simplified removal of excess reagents and byproducts through rinsing with a solvent; and (3) favoring rapid coupling kinetics due to continuous reactant excess on a new grafting site avoiding dilution effects [17]. In addition, a major advantage of flow SPPS is the ability to integrate several online modules for versatile control of some experimental parameters or follow-up of the reactions. For example, online coupling to UV–Vis absorbance detection allowed monitoring the progress of coupling and deprotection reactions in real time by the absorbance of the products [23], without interrupting the synthesis. A complementary online measurement of internal pressure variation [24] identified changes in resin volume, due to its swelling during the coupling, or its contraction during Fmoc deprotection, or peptide aggregation on the resin. In another example, a high temperature (90 °C) loop for reagents activation was connected at the inlet side of the reactor [25–27].

In this context, we aimed at developing a rapid and simple to implement process to provide versatility in sequence synthesis. A continuous flow SPPS protocol was optimized to obtain the desired peptide sequences for further self-assembly of the peptide building blocks. Briefly, flow synthesis began with resin swelling, followed by *n* cycles of peptide coupling, *n* being the number of amino acids in the desired sequence, and a final rinse to contract the resin and remove it from the reactor. The resin was then transferred to a flask for peptide cleavage, side-chain deprotection, and peptide precipitation (Figure 2).

The development of this new SPPS in flow reactors was first inspired by previous studies in our laboratory (results not shown) and different technological difficulties were first resolved. The DMF flow rate for resin introduction was optimized at 0.8 mL·min^{-1} for 30 min, which was a compromise between rapid column packing and possible heterogeneities in the swollen resin at higher flow rate, impacting the synthesis efficiency. Then, the volume of the resin during the synthesis increased due to the elongation of the peptide on the resin, as evidenced by a higher back pressure. Therefore, the system was optimized with a fixed-end column, instead of a piston; once the resin had swollen, it was manually packed with sand to hold it in place, so that the resin could swell freely during the synthesis. Finally, in conventional SPPS protocols, a final rinsing of the resin with CH_2Cl_2 is used to remove DMF, which may interfere with the final peptide cleavage step. However, the resin (ChemMatrix resin) used in this project swelled even more in CH_2Cl_2 than in DMF [28], leading to high back pressure. When optimizing our protocol, CH_2Cl_2 was replaced by Et_2O to rinse the resin directly, as well as to contract and remove the resin from the column. To the best of our knowledge, except for an application note, belonging to the Vapourtec® company, and one study on the development of SPPS on a microfluidic chip [29], the peptide cleavage step was rarely performed in continuous flow. Typically, the resin is removed from the reactor and any residual solvent is evaporated under vacuum before cleavage. It is also worth mentioning that all resins in the market swell almost twice as much in TFA (which is used for the deprotection step) as in organic solvents conventionally used in SPPS. In a flow reactor, this rapid and significant swelling is likely to create strong back
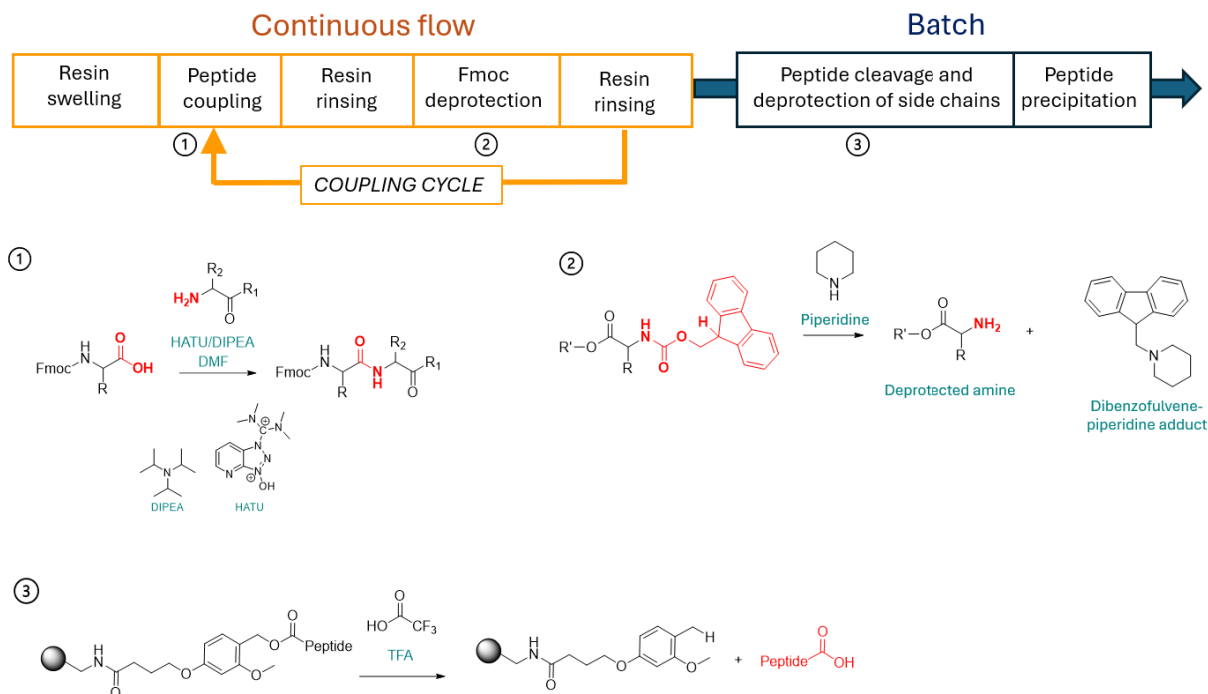
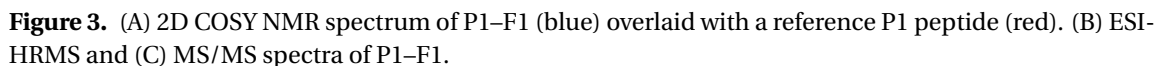**Figure 2.** Chemical reactions involved in peptide synthesis and workflow.

pressures. We therefore developed this final cleavage step in batch.

The product of this first synthesis (P1–F1) was analyzed by NMR (Figure 3A), and compared to a reference product, indicating that the sequence is missing amino acids, most likely serine (S = Ser) and aspartic acid (D = Asp). These are the first two amino acids added during SPPS, suggesting that the bonding to the resin was not as effective as expected. As structural analysis of the product by NMR alone was insufficient to establish the peptide composition, HRMS and MS/MS analyses were also carried out, revealing a mixture of peptide sequences in the product (Figure 3B and C). In particular, three truncated sequences were identified from ions detected in positive ionization mode: VVVVVVKKGR (calc. 1081.7, found 541.9 ($Z = 2$), 361.6 ($Z = 3$), 271.4 ($Z = 4$)), VVVVVVKKGRD (calc. 1196.8, found 599.4 ($Z = 2$), 399.9 ($Z = 3$), 300.2 ($Z = 4$)) and VVVVVVKKGRDS (calc. 1283.8, found 642.9 ($Z = 2$), 428.9 ($Z = 3$), 322.0 ($Z = 4$)).

Therefore, the raw product obtained in this first step did not contain the complete sequence and the first amino acids added during the synthesis were missing. Moreover, although structural analysis of the product by NMR and MS can identify the composition of the different peptide sequences, these classical characterization methods have their limitations. Indeed, the analysis of peptide NMR and HRMS spectra is particularly complex and time-consuming, especially for mixtures of sequences.

To guide optimization of P1 synthesis, the use of faster and more resolutive analytical methods that required little or no sample preparation was essential. The sensitivity of MS makes it the detection method of choice in proteomic analysis, but it has to be coupled with a separative method to easily characterize peptide sequence mixtures. Reversed-phase HPLC (RP-HPLC) is classically employed for either peptide characterization or purification. However, some peptide mixtures of similar polarities may co-elute, highlighting the need for complementary analytical methods to assess synthetic peptide purity. Compared to HPLC, CE offers higher separation selectivity and efficiency, lower reagent and sample consumption, lower waste generation, and shorter analysis time. Furthermore, CE selectivity is based on differential electrophoretic mobilities, according

Figure 3. (A) 2D COSY NMR spectrum of P1–F1 (blue) overlaid with a reference P1 peptide (red). (B) ESI-HRMS and (C) MS/MS spectra of P1–F1.

to the charge over size ratio of the compounds, instead of differential interactions with a stationary phase for HPLC. Coupled to the high sensitivity of the MS detection with ESI interface, a soft ionization mode, molecular masses and structural information can be obtained [30]. In 1994, CE coupled to MS by an electrospray ionization–desorption interface (CE-ESI-MS) was developed for the analysis of a synthetic short fragment of heregulin-β peptide (1959.8 Da) [31]. While HPLC evidenced a single peak in the chromatogram, CE-ESI-MS proved the presence of two peaks, corresponding to the expected peptide along with a dehydration product. An efficient separation of a mixture of synthetic gonadotropin releasing hormone (GnRH) decapeptides, which could not be resolved by HPLC, was also successfully performed by CE-ESI-MS [32]. A CE-ESI-MS qualitative identification of short peptide portions of the extracellular domain of a glycoprotein growth factor was performed in the mg·mL^{-1} concentration range [33]. Other developments with CE or CE-MS, either offline or inline, are described for applications in proteomics [34], peptide therapeutics [35] or design of cyclic peptides [36] among others, but to our knowledge, no other work has been reported so far on CE-ESI-MS for purity assessment and sequence check of synthetic peptides at low concentration level (0.1 mg·mL^{-1}).

Therefore, a CE-ESI-MS characterization method was developed in parallel to optimize the synthesis and obtain the complete sequence with better yield and purity [37]. This synergistic contribution may overcome the deficiencies evidenced previously on the peptide synthesis. The analysis of the products of P1–F1 synthesis evidenced six main peptide sequences missing the first amino acids that should be anchored to the resin (Figure 4). These initial results highlight the powerful efficiency of CE separation coupled to the efficient structure determination of MS, as CE-ESI-MS proved the presence of six truncated sequences, whereas previous results with HRMS and MS/MS only determined three of them.

Optimization of the synthetic workflow was then performed by CE-ESI-MS characterization. Figure 5 illustrates the three main peptide sequences that were identified at each step of this optimization. As the first amino acids that should be anchored on the resin were missing, a new protocol was tested including a longer residence time by decreasing the flow rate (from 2.5 to 1 mL·min^{-1}) (P1–F2). However, the last two or three amino acids were still missing. For each amino acid, two successive coupling solutions were then percolated through the reactor ("double coupling" of the amino acids). According to CE-ESI-MS characterization of P1–F3, an improvement of the synthesis occurred, as only
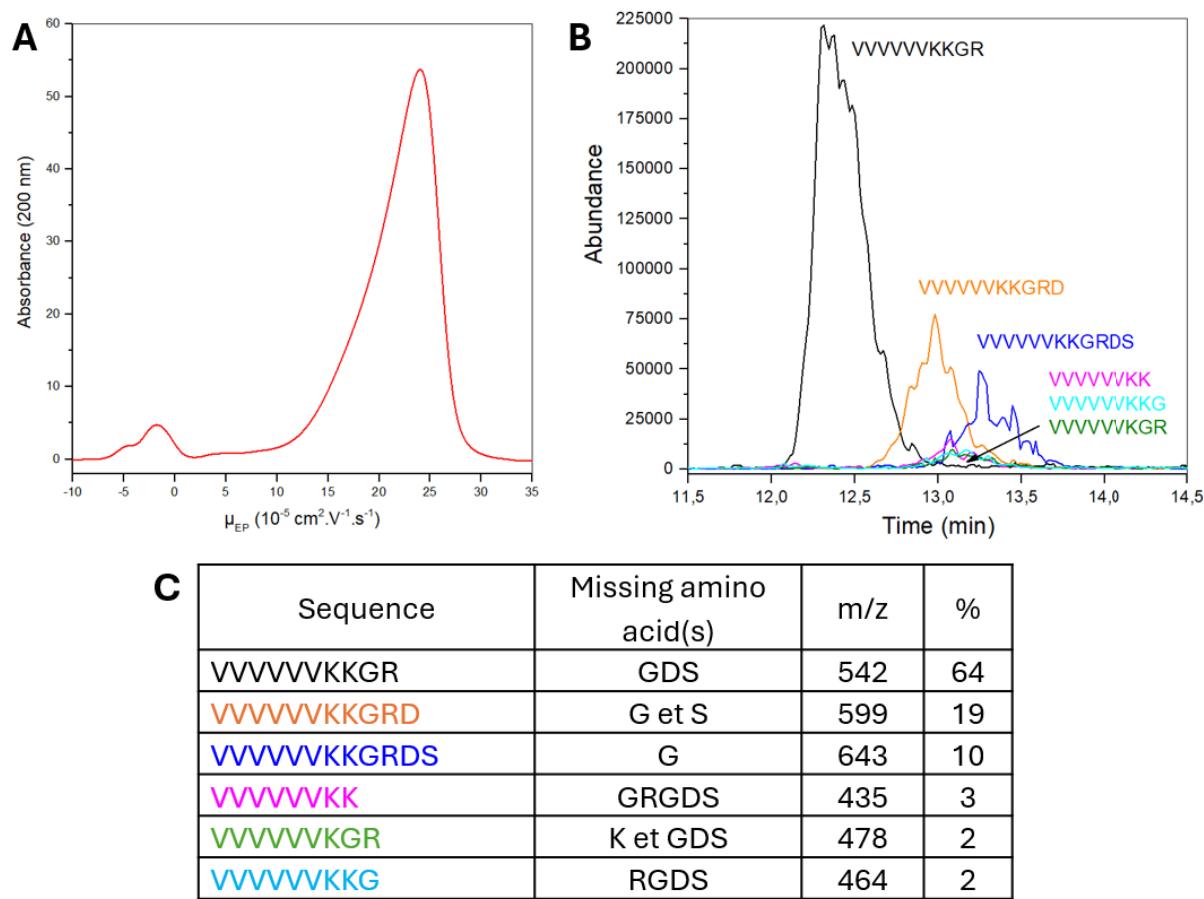
Figure 4. (A) CE-UV electropherogram of P1–F1 in 20 mM ammonium formate BGE (pH 3.7). (B) Extracted-ion signals from the total ion CE-ESI-MS electropherogram at specific m/z values summarized in (C). (C) Identification of the different sequences in P1–F1, with their corresponding missing amino acids and their relative abundance in the sample.

the first amino acid (S = Ser) was still missing in one sequence. This could be due to a difference of reactivity between the resin's linker and the amino acids. In one case, during anchoring to the resin, the carboxylic acid of the amino acid reacted with an alcohol function on the linker. In the other case, during the coupling between two amino acids, the carboxylic acid reacted with an amine, which is more nucleophilic than an alcohol. To make the alcohol on the linker more nucleophilic, it must be deprotonated with a strong base to form the alkoxide. In this first protocol, N,N-DiIsoPropylEthylAmine (DIPEA) was used combined with (dimethylamino)-N,N-diméthyl(3H-[1,2,3]triazolo[4,5-b]pyridin-3-yloxy)méthaniminium hexafluorophosphate (HATU)

to couple the first amino acid with the resin. As they did not seem to be strong enough to deprotonate the alcohol function, they were replaced by N,N'-DiIsopropylCarbodiimide, catalyzed by 4-DiMethylAminoPyridine (DIC/DMAP), a combination commonly used for grafting onto such resin [38,39]. However, HATU/DIPEA was retained for the other peptide couplings, as the DIC/DMAP has disadvantages such as lower yields, side reactions and racemization of the amino acid [40]. Thus, the synthesis protocol was modified to differentiate the resin grafting step from the peptide coupling one. The attachment of serine (S = Ser) to the resin was carried out as a double coupling, using the new DIC/DMAP reagents. The
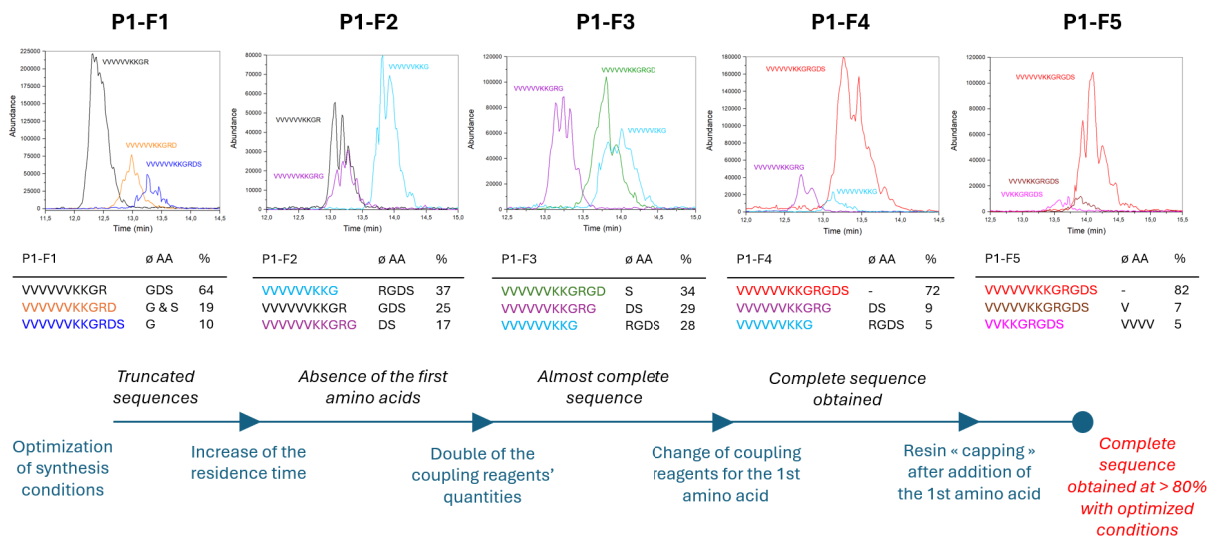
Figure 5. Summary of the various synthesis optimizations, guided by CE-ESI-MS characterization of the crude P1 products synthesized by continuous flow. For each synthesis, the three principal sequences were identified and their percentage are presented.

other peptide couplings were carried out as single couplings, with HATU/DIPEA. This choice was made to reduce the quantity of reagents and to evaluate the efficiency of the new binding conditions of the first amino acid on the resin.

This protocol (P1–F4) allowed to obtain the expected peptide sequence with 72% purity. The co-existence of truncated sequences could be explained by the fact that, after the 1st amino acid was anchored on the resin, the remaining functions on the surface of the resin are still accessible for the subsequent introduced amino acids. Blocking these free functions would potentially prevent the formation of these truncated sequences. Therefore, a final synthesis (P1–F5) was optimized by adding a blocking step ("capping" of the resin) for unreacted grafting sites on the resin with acetic anhydride (Ac_2O) after the anchoring of the first amino acid.

Again, CE-ESI-MS analysis of the products generated by this new protocol showed an increase of the purity of the expected peptide sequence up to 82%. This time, residual remaining truncated sequences were mostly related to missing amino acids in the end of the sequence, due to a non-quantitative peptide bond formation with the hydrophobic valines. This result validates the interest of adding a capping step

to the protocol.

Thanks to the synergistic contribution of synthesis and analytical developments, the peptide synthesis in continuous flow could be improved in several ways. The modulation of the flow allowed improving the efficiency while preserving a reduced time for synthesis; the coupling efficiency could be further enhanced by identifying the limiting step (anchoring to the resin) for which "double coupling" was implemented while changing the reactants. Finally, capping the resin, after the first amino acid has been grafted, allowed optimization verified by CE-ESI-MS characterization, enabling a peptide coupling cycle to be completed in less than 30 min. The entire sequence from resin swelling to peptide precipitation could be achieved in three days. With a rudimentary SPPS system in continuous flow, a significant improvement of the time for the complete synthesis has been achieved, compared to batch synthesis, which takes several weeks. This reduced time will be particularly important when modifications to the amino acid sequence are required to study the influence of the sequence nature on self-assembly. For this, it will be necessary to rapidly synthesize a library of modified sequences. In addition, the synthesis has been optimized on a small scale (200 mg resin), but the protocol is perfectly suited for

scale up and producing peptides in larger quantities. A miniaturization of the SPPS could also be considered in the future, to transfer the current millifluidic process to the microfluidic scale, where heat and mass transfer will be improved, that would reduce the time for the complete synthesis, and enable even faster optimization of operating conditions [41]. All the main characterized sequences in the product mixture contain RGD, the $\alpha v\beta3$ integrin targeting motif, and at least two valines capable of generating self-assembly of the peptide by hydrophobic interaction. Therefore, their self-assembly without purification may lead to mixtures of nanostructures, which may be compatible with their future use.

4. Efficient peptide functionalization with a MRI contrast agent guided by electrophoretic separations coupled to mass spectrometry

Magnetic Resonance Imaging (MRI) is one of the most widely used medical imaging methods to diagnose pathologies, including cancer. It is a non-invasive method based on the magnetic relaxation of nuclear spins of protons in water molecules, enabling tissue structure to be imaged. When image contrast is insufficient to differentiate between healthy and diseased tissue, an imaging probe, often a gadolinium complex (Gd), is injected to enhance contrast by increasing the magnetic relaxivity of water molecules.

Our strategy consisted of functionalizing the peptide sequence with a gadolinium complex, as Gd-Based Contrast Agents (GBCA) are the most used Contrast Agents (CA) in clinical MRI [42], and then formulating the self-assembly of the Gd complex functionalized peptide. Therefore, few strategic points had to be considered: the functionalization should be performed to preserve the pH-sensitive self-assembling properties, the active targeting by the RGD sequence, and the positioning of the MRI probe in the vicinity of the nanoobject surface, for an efficient MRI response.

For more than 20 years, GBCAs have been developed to bind to different ligands, such as antibodies, proteins, peptides, aptamers, polysaccharides, etc. [43]. In this context, peptides could be easily functionalized thanks to the diversity of their functional groups (amine, carboxylic acid, thiol) allowing for many bioconjugation strategies including click chemistry, peptide coupling and other chemoselective reactions [8,44]. In the peptide sequence P1, the self-assembly process leads to internalization of the primary amines, therefore their functionalization could impede the self-assembling process when functionalized. The two available carboxylic functions, the terminal carboxylic acid and the aspartic side chain, could be functionalized by the formation of an amide bond through peptide coupling with an amine. However, a peptide polycondensation could occur between the amines and the carboxylic acids present in the sequence. To avoid side reactions, a strategy with temporary protection groups on the peptide could be developed, however complicating the synthesis of the conjugate and lowering conjugation yields [44]. As the peptide functionalization should be specific, click chemistry appears as an interesting alternative, providing fast reactions and high yields. Particularly, a thiol-maleimide bioconjugation strategy could be developed, as maleimides react, without heat or catalytic processes, specifically with thiols, forming thiosuccinimides [45,46].

For this purpose, the rational design of a peptide sequence for developing theranostic agents consisted of modifying the initial peptide sequence P1 (VVVVVVKKGRGDS) by including a cysteine (C = Cys), with a thiol function, to facilitate its functionalization by a thiol-ene reaction with a chelating ligand, followed by complexation with Gd [47] (Figure 6A). This new designed sequence P2 (VVVVVVKKGRGDCS) provided a cysteine positioned in the hydrophilic head, just before the terminal amino acid, therefore close to the surface of the self-assembled nanostructure and preserving the RGD sequence. The selection of the ligand was made based on an efficient and specific functionalization and a strong complexation to Gd to avoid its leakage during theranostic applications. Therefore, cyclic DOTAGA ((2-(4,7,10-tris(carboxymethyl)-1,4,7,10-tetraazacyclododecan-1-yl) pentanedioic acid) was selected as the complexing agent for its high complexation constant ($\log K = 24.78$) and thermodynamic stability to Gd^{3+} chelator [48] (Figure 6B).

Two strategies were envisioned for this functionalization: either functionalizing the peptide sequence before self-assembly or functionalizing the peptide
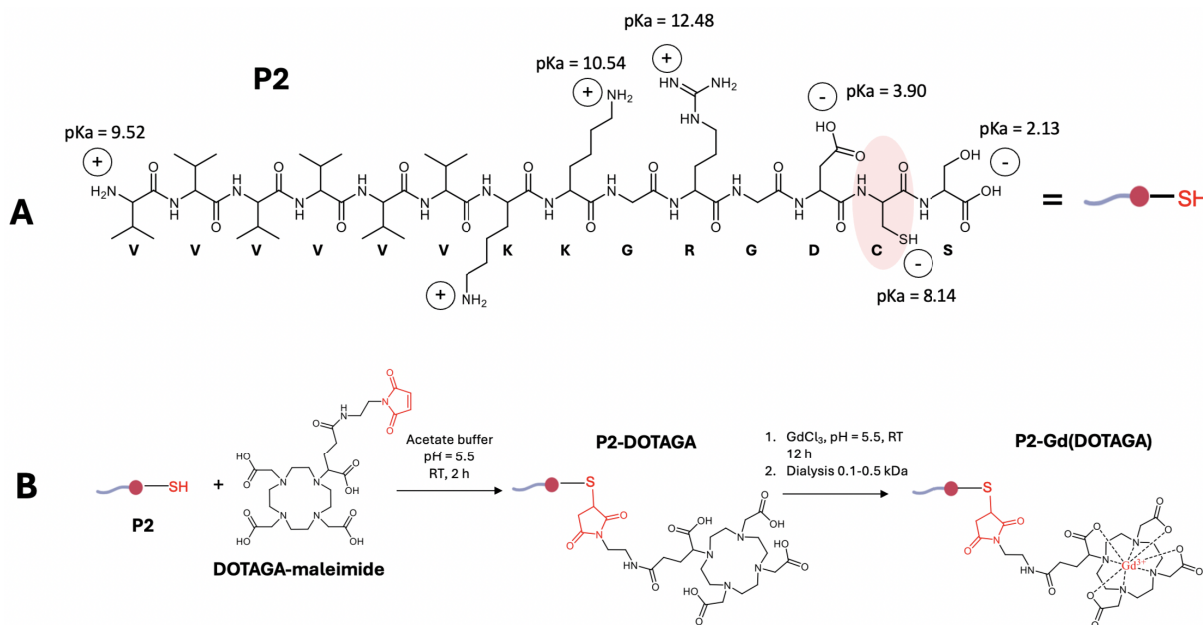
Figure 6. (A) Molecular structure of P2 peptide, with pK_a values of ionizable functions. (B) General scheme of the functionalization of P2 with DOTAGA via thiol/maleimide reaction, followed by Gd complexation, in 20 mM acetate buffer (pH 5.5). Adapted from Ref. [47].

self-assembly. The first strategy was preferred as it would allow a better monitoring of the functionalization step and to be able to better control the number of Gd-DOTAGA on the final nanotheranostic agent, without destabilizing the preformed supramolecular nanostructures. Indeed, to avoid Gd-DOTAGA crowding of RGD motifs on the surface of the self-assembled nanostructure, co-assemblies between non-functionalized and functionalized peptides were explored (Figure 7).

Acidic conditions were then necessary for the whole synthesis process to preserve the peptide in its monomeric form. Furthermore, enriched by our experience in efficient optimization of peptide synthesis followed by an electrokinetic method, a synergistic contribution of a new CE-ESI-MS development to follow the functionalization step and purification check was undergone.

The functionalization consisted of a two steps procedure: (1) mixing DOTAGA-maleimide (DOTAGA-mal) with the peptide solution (P2), dissolving in 20 mM acetate buffer (pH 5.5), at different molar ratios (0.1 equiv, 0.15 equiv, 0.2 equiv or 1 equiv), and stirring at room temperature for 2 h; (2) fol-

lowed by addition of Gd (10 mM GdCl$_3$ solution) to the previous solution, 4.5 equiv compared to the amount of DOTAGA-mal added previously, and stirring overnight at room temperature. The resulting solution was, in few cases, dialyzed with 20 mM acetate buffer (pH 5.5) with a membrane of 0.1–0.5 kDa cut-off, to eliminate the excess of Gd. This procedure was optimized at each step thanks to CE with dual UV and MS detection [47].

In a first step, the DOTAGA-maleimide (DOTAGA-mal) functionalization on the thiol present in the peptide was performed in a 1:1 ratio (DOTAGA-mal/thio-peptide). The electrophoretic mobilities of the resulting crude product (P2-DOTAGA) without dialysis, along with the starting materials (P2 and DOTAGA-mal) were determined by CE-UV (Figure 8A). They were coherent with the global charge of each species in the background electrolyte (20 mM ammonium acetate, pH 5.5). An electrophoretic mobility around 20×10^{-5} cm$^2 \cdot$V$^{-1} \cdot$s^{-1} was determined for P2 (black line) in accordance with a +2 charged species; around -30×10^{-5} cm$^2 \cdot$V$^{-1} \cdot$s^{-1} for DOTAGA-mal (blue line), that is expected to be twice negatively charged [49,50]. The crude mixture pre-
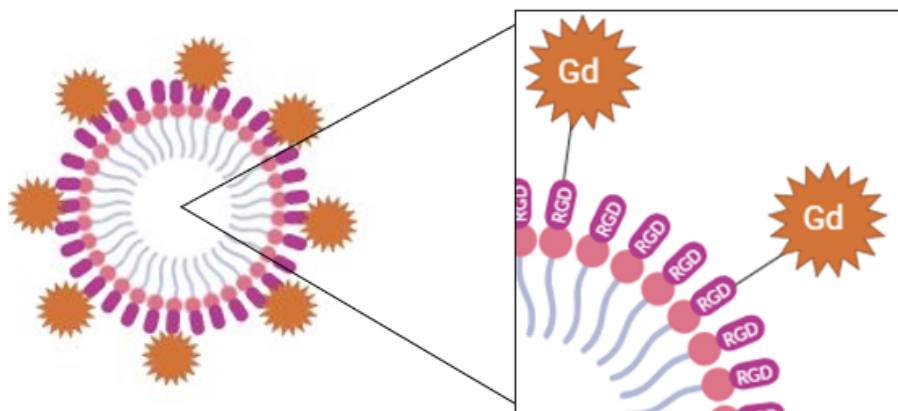
Figure 7. Scheme of the co-assembly structure from P2 and P2-Gd(DOTAGA). Adapted from Ref. [47].

sented an intense peak at -2.5×10^{-5} cm$^2 \cdot$V$^{-1} \cdot$s^{-1}, expected to be the one of P2-DOTAGA conjugate along with a small peak at around -30×10^{-5} cm$^2 \cdot$V$^{-1} \cdot$s^{-1} corresponding to excess DOTAGA-mal. The attribution of the peaks was confirmed by CE-ESI-MS (Figure 8B and C) on the crude mixture, thanks to the extracted ion electropherograms from the total ionic current (black line) of m/z = 682, 723 and 599, corresponding to specific ions of P2-DOTAGA, P2 and DOTAGA-mal, respectively. The large peak corresponds to P2-DOTAGA (full red line), confirming the success of the functionalization reaction in just 2 h, with the presence of P2 (full black line) and DOTAGA-mal (full blue line) being in little abundance, 4% and 2% respectively.

As our aim was to formulate direct co-assemblies between non-functionalized and functionalized peptides, the synthetic procedure was then performed with different molar ratios (0.1 equiv, 0.15 equiv or 0.2 equiv) between DOTAGA-mal and P2. This permitted obtaining mixtures of P2 and P2-DOTAGA conjugates, with relative amounts of functionalized peptide of 10%, 15% and 20%, labelled P2-DOTAGA10, P2-DOTAGA15 and P2-DOTAGA20, respectively, that could then be directly formulated, without a purification step, therefore with a gain in time. The rate of functionalization was monitored by CE-ESI-MS on the crude mixture without dialysis (Figure 9). For all three P2-DOTAGA samples, the UV signals evidenced the peak of P2-DOTAGA at around neutral mobility and the one of P2 at 15×10^{-5} cm$^2 \cdot$V$^{-1} \cdot$s^{-1}, while no peak of DOTAGA-mal (expected at -30×10^{-5} cm$^2 \cdot$V$^{-1} \cdot$s^{-1}) was seen,

confirming a 100% grafting rate of DOTAGA whatever the initial P2/DOTAGA-maleimide ratio. Experimental functionalization rates of the mixtures were then calculated from each peak area, taking into consideration any dilution effect, leading to 11%, 19% and 22% for P2-DOTAGA10, P2-DOTAGA15 and P2-DOTAGA20, respectively, which are consistent with the theoretical ones.

Gd complexation was then performed on these mixtures, leading to P2-Gd(DOTAGA)10, P2-Gd(DOTAGA)15 and P2-Gd(DOTAGA)20 (Figure 10A), and the products were characterized by CE-ESI-MS. Two main peaks were shown for the three mixtures on the total ion signal, identified as P2 for the peak at 14 min (m/z = 723 and 482, [M+2H]$^{2+}$ and [M+3H]$^{3+}$, respectively) and as P2-Gd(DOTAGA) for the one at 15 min (m/z = 733, [M+3H]$^{3+}$), according to the single ion signals (Figure 10B for Gd(DOTAGA)10, as an example). No peak of P2-DOTAGA (m/z = 695, [M+H+Na+NH$_4$]$^{3+}$) was evidenced, proving the efficiency of the complexation step and confirming that all the DOTAGA grafted on P2 are under Gd(DOTAGA) complex form. This two-step functionalization strategy afforded mixtures of P2 and P2-Gd(DOTAGA) with a very simple procedure without purification, in a short time (14 h), and that can directly be used for future co-assemblies in the formulation of nanovectors. Figure 10B represents the CE-ESI-MS for Gd(DOTAGA)10, as an example.

The stability of P2-Gd(DOTAGA)10, P2-Gd(DOTAGA)15 and P2-Gd(DOTAGA)20 dispersions was assessed by CE-ESI-MS, in the same condi-
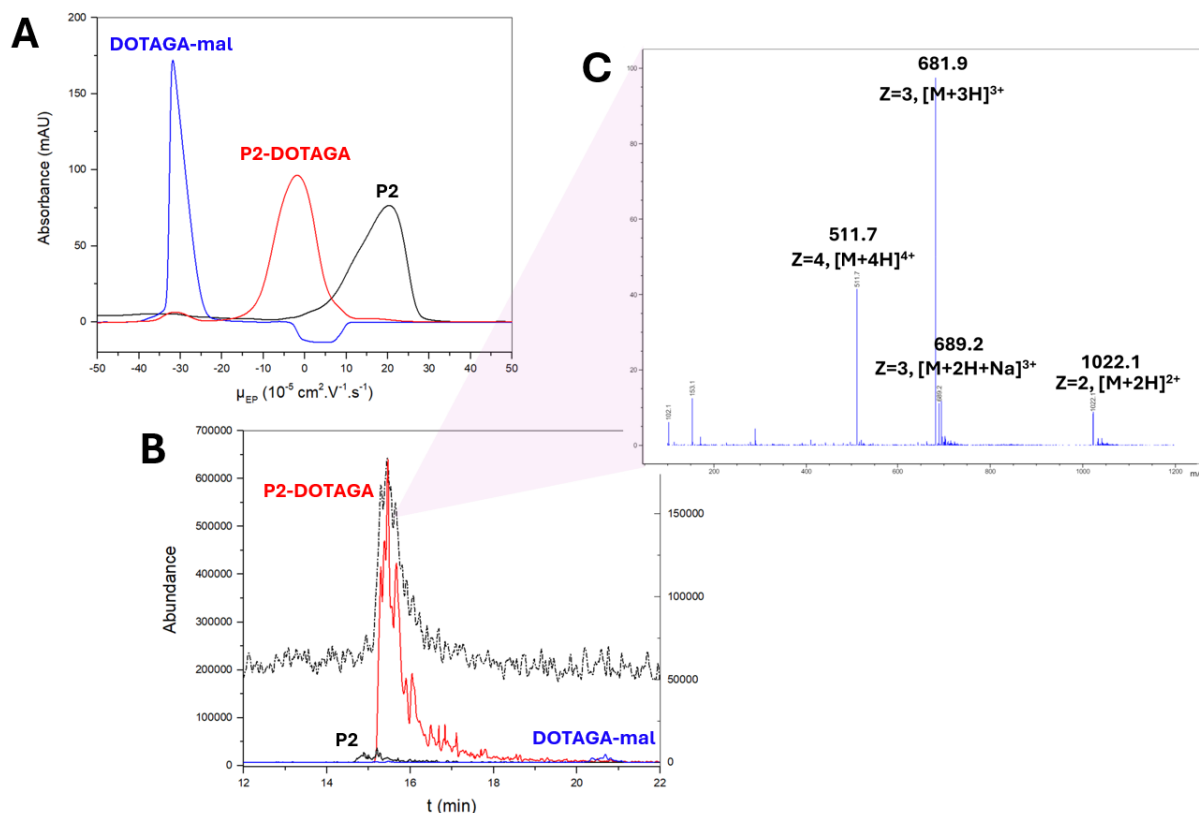
Figure 8. (A) CE-UV electropherograms of DOTAGA-maleimide (DOTAGA-mal) (blue), P2 (black) and the crude functionalization product (red), in 20 mM ammonium formate buffer (pH 5.5). (B) CE-ESI-MS electropherogram of the reaction product. Total ion signal (m/z 100–1200, black line) and extracted ion signals specific of P2-DOTAGA (red), of P2 (black) and of DOTAGA-maleimide (blue). (C) Extracted mass spectrum from the total ion electropherogram (black line in (B)) of the reaction product under the peak at 15.5 min. Adapted from Ref. [47].

tions as previously after 1 month storage at 4 °C. On the one hand, the free thiol moieties on the non-functionalized peptide are expected to form disulfide bonds leading to dimers. On the other hand, Gd decomplexation is unlikely due to the high complexation constant ($\log K = 24.78$) [48], but hydrolysis of the thiosuccinimide moiety could occur on the functionalized peptide [51]. CE-ESI-MS characterization confirmed that non-functionalized peptide monomers had begun to form disulfide bonds after 1 month in solution. However, the higher the functionalized peptide ratio is in the mixture, the less this aging process is observed. No thiosuccinimide hydrolysis, Gd decomplexation or other degradation of the peptide sequence was evidenced. Bearing in mind the further use of these peptide products as structural building blocks to form self-assembled nanostructures, it may be worthwhile to study the impact of the formation of peptide dimer, when stored, on the self-assembly. Furthermore, optimized storage procedures could be studied to limit sample transformation through time.

In summary, a Gd(DOTAGA) complex was functionalized on P2 (VVVVVKKGRGDCS) by the addition of thiol function to the maleimide. A DOTAGA was first bound to the peptide, followed by complexation of the Gd^{3+} ion by the ligand. Again, CE-ESI-MS appeared to be an appropriate analytical method for functionalization and aging studies of peptide conju-
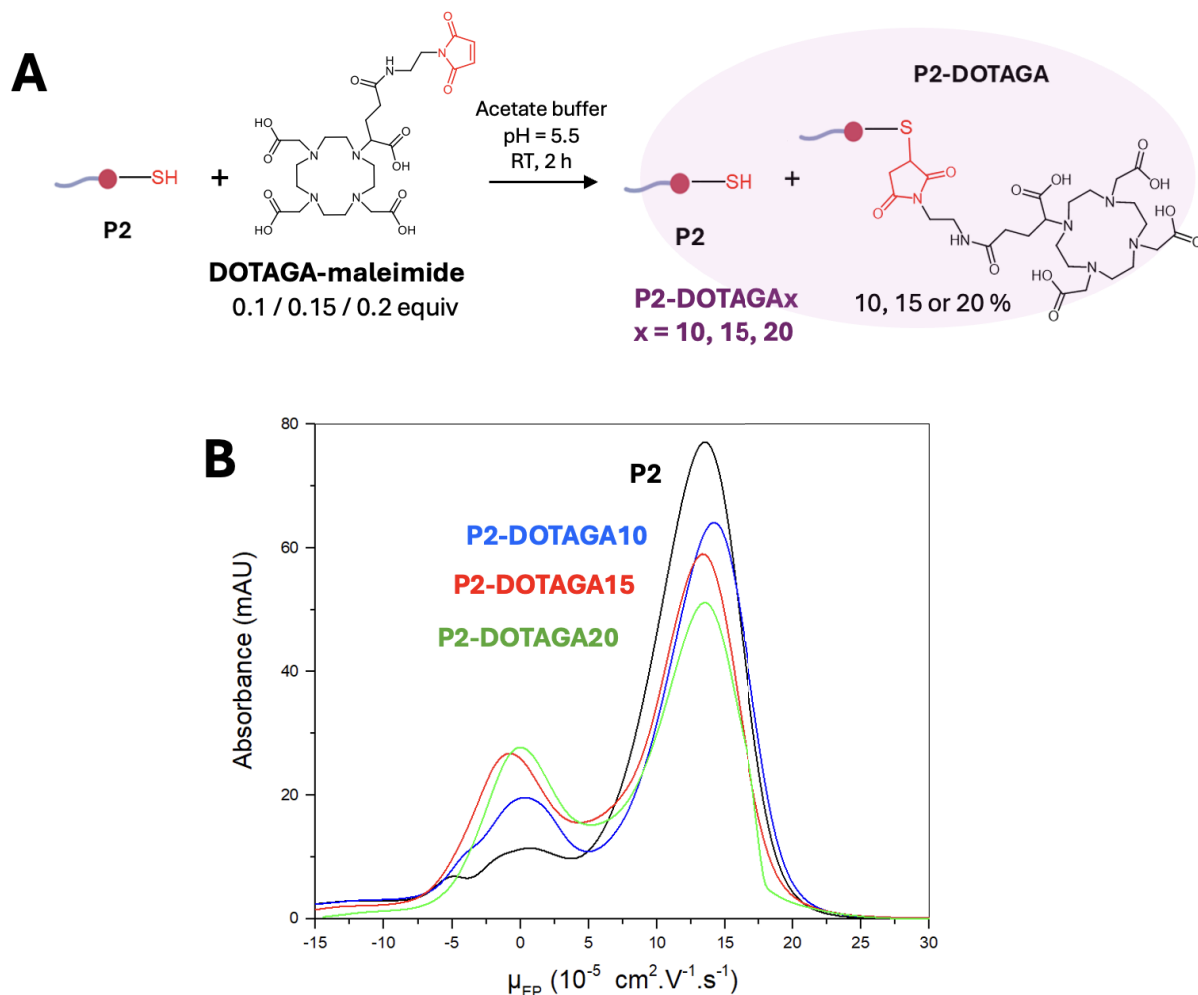
Figure 9. (A) Reaction scheme of the functionalization of P2 with different amounts (0.1, 0.15 and 0.2 equiv) of DOTAGA-maleimide in 20 mM acetate buffer (pH 5.5), to form mixtures of P2 and 10, 15 and 20% of P2-DOTAGA, called P2-DOTAGA10, P2-DOTAGA15 and P2-DOTAGA20, respectively. (B) CE-UV electropherograms of P2 and mixtures P2-DOTAGA10, P2-DOTAGA15 and P2-DOTAGA20 in 20 mM acetate buffer (pH = 5.5). Adapted from Ref. [47].

gates based on simplicity, rapidity, low sample consumption and direct analysis without requirement for sample preparation.

5. Formulation and understanding of peptide self-assembly guided by a combination of complementary analytical and physical methods

Peptide self-assemblies are essentially based on weak interactions [52], the combination of which leads to the formation of well-organized and stable nanostructures. These structures can be designed to change the shape in response to a stimulus, such as a variation of the pH, enzymatic activity, high ROS concentration or a change in temperature [53], which is of particular interest for controlling the drug delivery, where we seek to trigger the release of active ingredients at a specific site, such as a tumor.

A deep understanding of peptide self-assembly would be of great interest for both the design of new peptide sequences and the optimization of the for-
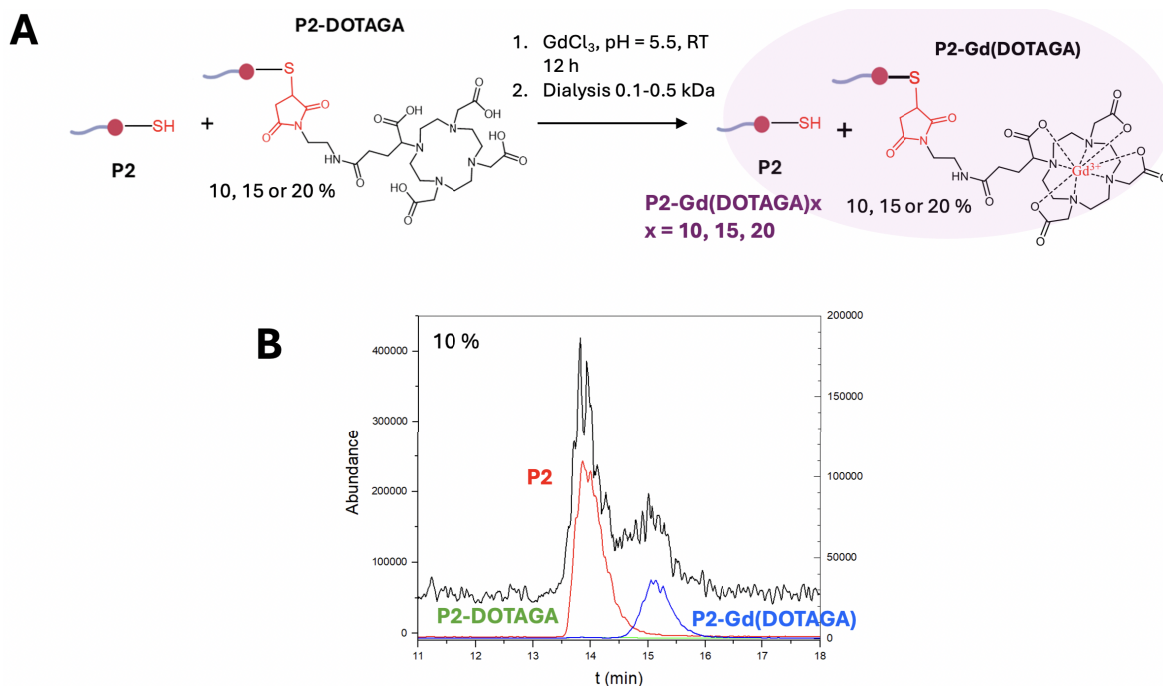
Figure 10. (A) Reaction scheme of the complexation of Gd by P2-DOTAGA, to form mixtures of P2 and 10, 15 and 20% of P2-Gd(DOTAGA) in 20 mM acetate buffer (pH 5.5). (B) CE-ESI-MS electropherogram of mixture P2-Gd(DOTAGA)10, with the total ion signal (black, m/z 400–1150) and single ion signals at m/z values specific of P2 (red), P2-DOTAGA (green) and P2-Gd(DOTAGA) (blue). The left and the right axes correspond to the abundance for the total ion signal and the single ion signals, respectively. Adapted from Ref. [47].

mulation conditions [54]. Therefore, several complementary methods were used for characterizing the self-assembly of the previously synthesized peptides: pH measurement, Dynamic Light Scattering (DLS), Transmission Electron Microscopy (TEM), Circular Dichroism (CD), CE-UV and Taylor Dispersion Analysis (TDA) in capillary format. The strategy was to test the peptides P1 and P2, presenting no functionalization, along with the functionalized peptide P2 (P2-DOTAGA), and the mixtures of P2 and P2-Gd(DOTAGA) (P2-Gd(DOTAGA)10, P2-Gd(DOTAGA)15 and P2-Gd(DOTAGA)20), to increase complexity in nanostructures and gain insights into the involved mechanisms.

A first attempt to reach P1 self-assembling was realized according to Liang et al. [18] by dissolving P1 at 0.05 or 0.5 g·L^{-1} in water. However, no self-assembly was observed, probably due to the respective pHs of 4.5 and 3.5 of the sample solution. An increase in pH was then performed by progressive addition

of small volumes (20 µL) of 1 M NaOH, which led to precipitation when a pH value around 6 was reached. A second attempt consisted of a dialysis-assisted formulation, inspired by Liang et al. [18] was again unsuccessful. Therefore, a new P1 self-assembly pathway using rapid addition of NaOH was developed, with successive volumes of less than 20 µL of 1 M NaOH solution to avoid dilution effect, and a stable colloidal solution was obtained when the pH reached a value of 11. Knowing that the "Critical Micellar Concentration" was estimated at 0.02 g·L^{-1} [18], three P1 concentrations were tested (0.5, 1 and 2 g·L^{-1}) and DLS measurements evidenced nanostructures with average diameters of 50 nm and a polydispersity index (PDI) of 0.2 or below, indicating no correlation between self-assembly size and initial P1 concentration, in the 0.5 to 2 g·L^{-1} range (see Figure 11A for 1 g·L^{-1}). Aging studies with a period of 19 days proved a good colloidal stability for P1 solutions at 0.5 and 1 g·L^{-1}, with a preser-

vation of their intial size and dispersion medium pH, whereas the P1 solution at 2 g·L^{-1} underwent an increase in nanostructure hydrodynamic diameter up to 110 nm along with a decrease in pH to 10.3 after 14 days, leading to peptide precipitation. Decrease in pH could be explained by peptide amphoteric properties that may alter the pH of the dispersion medium at high concentrations with slow kinetics. Following these observations, self-assembly studies were continued at 1 g·L^{-1} where the sample appeared to be the most stable in terms of pH and nanostructure hydrodynamic size. TEM images were then performed by deposition of the sample on a copper grid coated with a carbon/Formvar film followed by deposition of an aqueous solution of uranyl acetate (2%) to color the sample and improve the image contrast, and finally air-drying of the grid. Images demonstrated short nanorods with lengths of 46.1 ± 12.2 nm and diameters of 9.2 ± 2.7 nm. To assess grid preparation without impairment of the self-assembly, cryo-TEM images were then performed, confirming the nanorods with the same dimensions (Figure 11B). The difference in size from DLS to TEM is expected and coherent. DLS measures the apparent hydrodynamic diameter of an equivalent spherical particle (as the detection angle in this study was of 173° with backscatter). Back scattering measured in DLS is sensitive to the largest dimension of non-symmetrical nanoobjets. TEM measures actual solid dimensions, associated with morphology.

To elucidate the interactions involved under these conditions in the nanostructuration of P1, circular dichroism (CD) measurements were carried out. For this purpose, P1 was either dissolved in water (pH = 3), in water with the addition of 2 equiv of NaOH (pH = 7) or 10 equiv of NaOH (pH = 11). At pH 3 and 7, a random coil conformation was evidenced, whereas a β-sheet structuration was observed for the solution at pH 11 (Figure 11C). It is very likely that the β-sheets are formed by inter-peptide hydrogen bonds at the polyvaline level, valine being an amino acid with a high propensity to form β-sheets [55]. The amine on the lysine side chain (pK_a 10.5) should be protonated at pH 3 or 7, leading to electrostatic repulsion that impedes β-sheet formations. Their deprotonation at pH 11 should eliminate this repulsion, allowing for self-assembling. In addition, the zeta potential of self-assembled P1 structures at pH 11 was measured, indicating a strong negative surface charge, with a

zeta potential value of -38 ± 9 mV. This result suggests that P1 self-assembles into a structure that exposes to the solvent negatively charged functions, i.e. the carboxylates of aspartic acid (D = Asp) and serine terminal acid (S = Ser), from the hydrophilic head of the sequence.

CE-UV experiments were carried out for in-depth characterization of P1 (1 g·L^{-1}), self-assembly (Figure 11D). In a 10 mM sodium phosphate separation buffer (pH = 11), P1 was separated, either dissolved in water (pH = 3) in its monomer form; or after addition of NaOH (10 equiv) to the previous solution, in its nanostructured form (pH = 11).

The electrophoretic profiles are similar, corresponding to a negatively charged species, with an electrophoretic mobility of -30×10^{-5} cm^{-2}·V^{-1}·s^{-1}, consistent with the one determined by zetametry at pH 11 ($-30 \pm 7 \times 10^{-5}$ cm^{-2}·V^{-1}·s^{-1}). Furthermore, these CE-UV characterizations reveal a fast self-assembly kinetics, compared to the time of separation. Indeed, P1, initially solubilized at pH 3, self-assembles during the separation in the capillary, due to the pH value (pH = 11) of the separation medium, this pH value being previously proved as efficient for peptide self-assembly.

All these combined physicochemical characterizations demonstrate the self-assembly of P1 at pH 11 into elongated, nanorod-like micelles.

The cylindrical morphology could be explained by the β-sheet interactions between the valines, leading to a stable nanostructure (Figure 12). Considering that an amino acid measures 3.4 Å [56], P1 would measure around 4 nm. This order of magnitude is consistent with a rod structure showing an estimated diameter of 9.2 ± 2.7 nm in TEM. This new structuration mechanism identified here for P1 is coherent with what was described in the literature with other peptide sequences. Wang et al. described the self-assembly of A9K into nanorods at pH 6, with lengths less than 100 nm [57]. The authors stated that the structuration could be due to β-sheets formation. However, they did not study the influence of pH on self-assembly of A9K, contrary to what has been studied in this work.

As indicated previously, another peptide sequence (P2) was designed to provide an additional cysteine (C = Cys) compared to P1, to facilitate the peptide functionalization with an MRI probe in view to combine smart drug delivery and imaging proper-
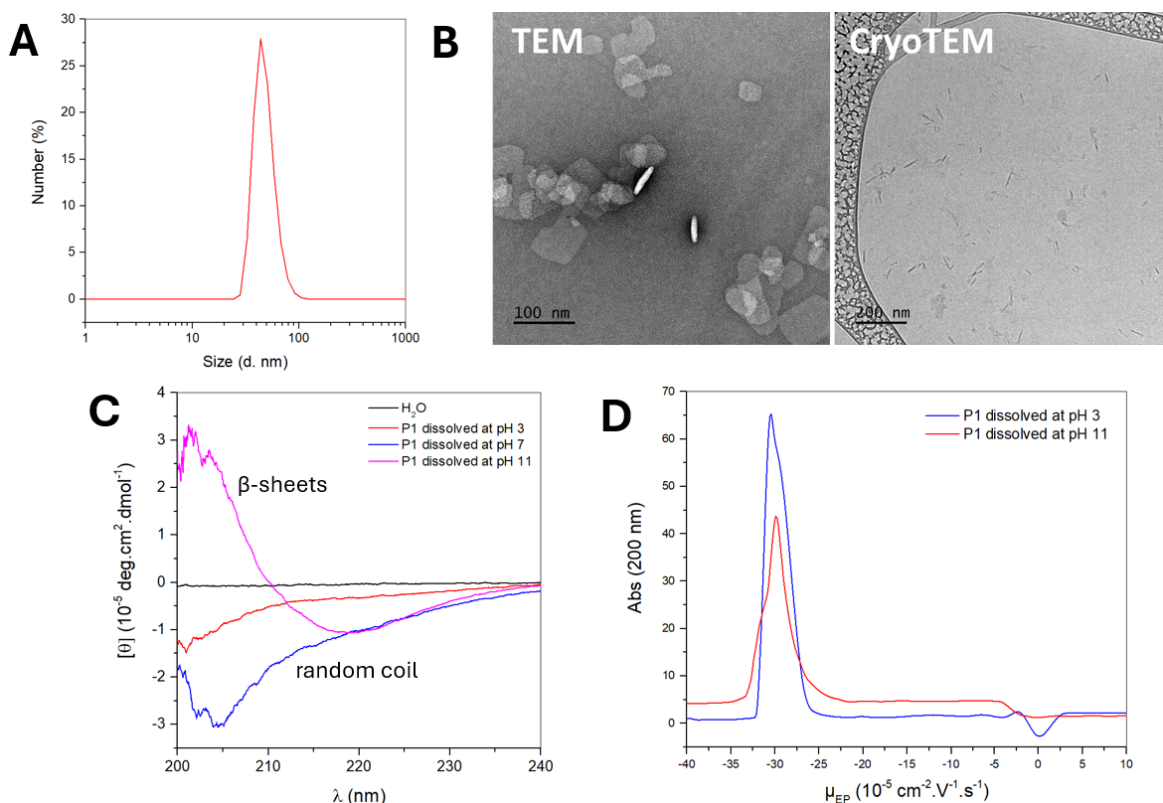
Figure 11. (A) Size distribution of self-assembled P1 (1 g·L^{-1}) at pH 11 obtained by DLS, in percentage of number of particles. (B) TEM and cryo-TEM images of self-assembled P1 at pH 11. (C) Circular dichroism spectra of P1 dissolved at pH 3, pH 7 and pH 11. (D) CE-UV electropherograms of P1 dissolved at pH 3 (blue) and pH 11 (red), analyzed in 10 mM sodium phosphate buffer (pH 11). Adapted from Ref. [54].
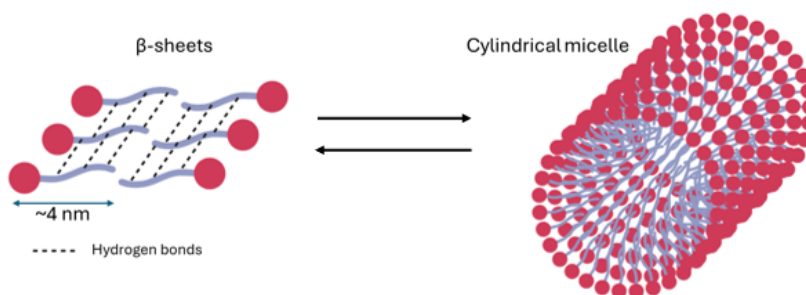
Figure 12. Proposed nanostructuring of P1 at pH ≥ 11, as a cylindrical nanorod stabilized by inter-peptide hydrogen bonds between polyvalines. Adapted from Ref. [54].

ties. Therefore, the self-assembly characterization of these new peptide sequences was carried out at a 1 g·L^{-1}, in the same way as for P1. The self-assembly of P2 or P2-DOTAGA was studied in a first step, followed by the co-assembly study of a mixture of P2 and P2-Gd(DOTAGA) at different ratios. All the samples were formulated at pH 11, according to the previously described protocol for P1 and characterized by combined methods.

Regarding P2, DLS measurements showed the

preservation of self-assembling properties, which is consistent with the fact that the presence of the cysteine (in the hydrophilic head of the peptide) must not interfere with the formation of β-sheets due to the polyvalines (Table 1). A monodispersed distribution was determined at a hydrodynamic diameter of 36 ± 6 nm (PDI = 0.16). Furthermore, TEM and cryo-TEM images revealed the presence of nanorods with a length of 27.2 ± 8.4 nm and a diameter of 7.3 ± 1.5 nm. A similar diameter and a smaller rod length was evidenced by TEM when comparing P2 and P1 (Table 1). An insignificant modification in hydrodynamic diameter was evidenced for P2 by DLS, compared to P1. This could be explained by the presence in P2 of the thiolate form of the cysteine at pH 11, leading to an additional negative charge, that could disrupt more rapidly the rod elongation than in the case of P1. To confirm these results, the diffusion coefficient of P2 was measured by Taylor Diffusion Analysis (TDA) performed in a capillary, leading to a value of $87.5 \pm 1.9 \times 10^{-11}$ m$^2 \cdot$s^{-1} (corresponding to a hydrodynamic diameter of 33.6 ± 0.6 nm) at pH 11, and a value of $18.9 \pm 15.7 \times 10^{-11}$ m$^2 \cdot$s^{-1} (corresponding to a hydrodynamic diameter of 3.40 ± 0.93 nm) at pH 5.5 (Table 1). The hydrodynamic diameter at pH 11 is the same as the one determined by DLS, reiterating P2 self-assembly. At pH 5.5, the hydrodynamic diameter indicates the presence of P2 in its monomeric form and is congruent with similar data from the literature (2.0 ± 0.2 nm measured by TDA for oxytocin, a 1 kDa peptide) [58]. Thus, DLS, TEM, cryo-TEM and TDA confirmed that P2 does indeed self-assemble into nanorods at pH 11, with similar dimensions to P1. The interest of TDA for such characterizations should be highlighted, as the monomeric form could be evidenced with TDA, whereas it was not possible with DLS.

To design the contrast agent based on P2 self-assembly, the latter was first functionalized with DOTAGA. P2-DOTAGA was formulated, and analyzed by DLS, which evidenced monodisperse nanostructures (PDI = 0.19) with a hydrodynamic diameter of 67 ± 22 nm. This proves that the self-assembly property of P2 is well preserved even after DOTAGA functionalization. Furthermore, the twice larger size of the P2-DOTAGA nanostructure compared to P2 could be explained by the steric hindrance generated by DOTAGA, but this larger size is not problematic as it remains within the desired size range (<100 nm) for biomedical applications.

The functionalized P2-DOTAGA was then complexed with Gd. Nonetheless, to avoid Gd(DOTAGA) crowding of RGD motifs at the surface of the self-assembled nanostructure, co-assemblies between functionalized (P2-Gd(DOTAGA)) and non-functionalized (P2) peptides were explored, in a ratio of 10, 15 and 20% of P2-Gd(DOTAGA) in the mixture. The choice of co-assembly ratios was made on the basis of the following criteria: (1) the presence of Gd at a minimum concentration is sufficient to generate good MRI contrast; (2) Gd(DOTAGA) is grafted close to RGD and is likely to decrease, or even prevent it from interacting with αvβ3 integrins. Thus, a co-assembly composed mainly of P2 was assumed to be rational.

For all three formulations, the hydrodynamic diameters measured by DLS are identical at around 40 nm, which is congruent with the values of P2 (36 ± 6 nm) and P2-DOTAGA (67 ± 22 nm) self-assemblies. TEM analysis also revealed nanorods with a length of 27.2 ± 8.3 nm and a diameter of 7.3 ± 1.5 nm (Table 2).

To delve deeper into the self-assembly characterization, CE-UV separation of the three formulations was performed in a separation medium at pH 11, with the same protocol as for P1. The sample was analyzed after preparation either at pH 5.5 (in ammonium acetate buffer, which corresponds to the medium in which the functionalization was carried out), where the sequences should remain in their monomeric form; or at pH 11, after addition of NaOH (40 equiv) as previously described.

For each of the three mixtures, the two solutions show electropherograms characteristics of negatively charged species, of very similar electrophoretic mobility values (-25×10^{-5} cm$^{-2} \cdot$V$^{-1} \cdot$s^{-1}) slightly lower than the ones obtained for P2 (-30×10^{-5} cm$^{-2} \cdot$V$^{-1} \cdot$s^{-1}), which is congruent with the difference both in size (evidenced by DLS) and charge (cysteine functionalization reduces the surface charge) of the formulations (Figure 13 for P2-Gd(DOTAGA)20). However, the solutions prepared at pH 5.5 should generate positively charged monomers. When injected in the capillary the sample at pH 5.5 migrates into a basic separation medium (pH = 11), leading to negatively charged nanostructures, due to self-assembly during the electrophoretic separation process. As for P2, the self-assembly mechanism kinetics was rapid compared

Table 1. Determination of the hydrodynamic diameter (D_H) by DLS and TDA, and length and diameter by TEM of the self-assembled P1 and P2

	DLS		TDA			TEM	
	D_H (nm)	PDI	pH	Diffusion coefficient (10^{-11} m^2·s^{-1})	D_H (nm)	Length (nm)	Diameter (nm)
P1	48 ± 11	0.14				46 ± 12	9 ± 3
P2	36 ± 6	0.16	5.5	19 ± 16	3 ± 1	27 ± 8	7 ± 2
			11	2 ± 1	34 ± 1		

PDI: PolyDispersity Index. Adapted from Ref. [54].

Table 2. Determination of the hydrodynamic diameter (D_H) by DLS, and length and diameter by TEM of the self-assembled P2 and P2-DOTAGA and the co-assembled P2-Gd(DOTAGA)x (x = 10, 15, 20)

|	DLS		TEM	
	D_H (nm)	PDI	Length (nm)	Diameter (nm)
P2	36 ± 6	0.16	27 ± 8	7 ± 2
P2-DOTAGA	67 ± 22	0.19	-	-
Co-assemblies				
P2-Gd(DOTAGA)10	38 ± 12	0.24	24 ± 6	8 ± 1
P2-Gd(DOTAGA)15	42 ± 9	0.25	22 ± 6	7 ± 1
P2-Gd(DOTAGA)20	41 ± 14	0.24	22 ± 6	8 ± 1

PDI: PolyDispersity Index. Adapted from Ref. [54].

to the separation process. The presence of shoulders on the peak shapes indicates a more complex equilibrium which is coherent with a more heterogenous sample due to random peptide co-assembly.

Therefore, these physicochemical characterizations prove the co-assembly of P2-Gd(DOTAGA) and P2, with different proportions (10, 15 and 20%) leading to self-assembled nanostructures of similar size and shape as those obtained only by self-assembly of P2. The strategy for developing these nanotheranostic agents was therefore successful in terms of nanostructuration. They could be further studied in terms of MRI properties.

6. Evaluation of Peptide-Gd(DOTAGA) conjugates as MRI contrast agents: a proof of concept

The principle of MRI is based on the nuclear magnetic resonance of protons in water molecules. Under the effect of a magnetic field oriented along
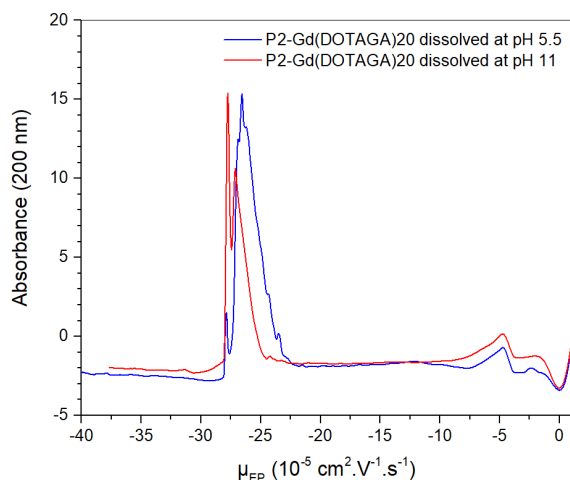
Figure 13. CE-UV electropherograms of P2-Gd (DOTAGA)20 dissolved at pH 5.5 (blue) or pH 11 (red), separated in 10 mM CAPS/ammonium buffer (pH 11). Adapted from Ref. [54].

the *z* axis, the spins of the protons all align themselves along this axis, either parallel or antiparal-

lel. Upon excitation of hydrogen nuclei of intrinsic water molecules and by the application of magnetic fields, 3D images of the proton spins are reconstructed, and two parameters related to the relaxation of the hydrogen nuclear spin are measured: the longitudinal and transversal relaxation rates, R1 and R2, respectively, which modulate the recorded signal. To enhance the contrast for a better visibility of the tissues structure, a contrast agent (CA) is usually administered intravenously to the patient to increase the contrast between diseased and healthy tissue, and to enable a more accurate diagnosis [59]. Proton relaxation is accelerated by dipolar interactions between the magnetic moments of a paramagnetic ion of the CA and the protons of the surrounding water molecules, resulting in shorter relaxation times T1 and T2 [60]. CAs are classified as either T1 or T2 agents. T1 agents generate a hypersignal and are generally gadolinium complexes, but can also be manganese complexes, for example Mn(II)-dipyridoxyl diphosphate (Mn(II)DPDP), which is the only clinically approved Mn(II) complex [61] or iron complexes [62]. T2 agents are compounds that generate a hyposignal and are based on iron oxide, most often in the form of superparamagnetic iron oxide nanoparticles (SPION) [63]. Each contrast agent is defined by a longitudinal relaxivity r_1 and a transverse relaxivity r_2, related to the longitudinal (1/T1) and transverse (1/T2) relaxation rates, respectively. The ratio r_2/r_1 indicates the property for the MRI contrast agent to be T1 type ($r_2/r_1 = 1$, bright intensity image) and to be a T2 type ($r_2/r_1 > 10$, darker intensity image) [60].

In this study the peptide sequences P2-DOTAGA were complexed with the Gd(III) ion, the paramagnetic metal ion with the highest number of single electrons (7 single electrons, $S = 7/2$). This property gives Gd a very high magnetic moment, justifying its use as an MRI contrast agent. As indicated above, the paramagnetic relaxation of water protons in the presence of a contrast agent arises from dipolar interactions between the protons' nuclear spins and the local magnetic field created by the spins of the single electrons of the paramagnetic ion. This magnetic field decreases with distance. There are two contributions to paramagnetic relaxation: those of the inner sphere and those of the outer sphere. In the case of Gd complexes, the inner-sphere mechanism is based on the interactions between the Gd^{3+}

ion and water molecules involved in its first coordination sphere. These water molecules exchange energy with other molecules in the medium, propagating the paramagnetic effect to the environment around the contrast agent. As for the external sphere mechanism, it concerns the paramagnetic effect of Gd on the water molecules diffusing around the complex [60].

Despite its advantages as an MRI contrast agent, free Gd(III) in the body is acutely toxic as it interferes with the operation at the calcium channels, which can lead to mitochondrial dysfunction, inhibition of neurotransmitters and muscle contraction [64]. In order to be used safely in vivo, Gd(III) is complexed by a polydentate organic ligand called a chelator, which can be either linear or cyclic. These ligands are designed to form thermodynamically stable Gd complexes with very high complexation constants (Log K of 25), to limit the release of Gd or transmetallation in the body. As a result, complexed Gd interacts little or not at all with tissues and is eliminated rapidly (>80% of the injected dose is eliminated after 24 h), limiting its accumulation in the body [65].

In 1987, gadopentetate dimeglulin Gd(DTPA) was the first Gd complex to be approved for clinical use and is still marketed today under the name of Magnevist®. Since then, other Gd complexes have been approved and have rapidly reached the market for use in MRI: Gd(DOTA) (Dotarem®), Gd(HP-DO3A) (Prohance®), Gd(DO3A-butrol) (Gadovist®), Gd(DTPA-BMA) (Omniscan®), Gd(EOB-DTPA) (Eovist®), Gd(BOPTA) (Multihance®) and Gd(MS-325) (Ablavar®) [42]. All these complexes are based on linear chelators such as DiethyleneTriamine-PentaAcetic acid (DTPA) or cyclic chelators such as 1,4,7,10-tetraazacyclododecane-1,4,7,10-tetraacetic acid (DOTA). The cyclic ligands derived from DOTA are preferred because they have the highest complexation constants with Gd, with log $K = 24.78$ for Gd(DOTA). However, the use of Gd complexes in vivo for cancer diagnosis remains limited by the lack of specific tumor cells targeting. Due to the low sensitivity of MRI (10 μM in blood) [66], large doses must be administered to patients, which can lead to side effects. As with other biomedical imaging modalities, the conjugation of Gd complexes with a peptide is one of the most widely exploited strategies in research for active tumor targeting. Between 2017 and 2020, more than a third of the MRI contrast agents

developed and reported in the literature were conjugated with one or more targeting peptides [67–69].

Although the active targeting of MRI peptide probes makes it possible to obtain more accurate and precise diagnoses, the size of peptide probes remains relatively small, leading to premature elimination of the product before it can fulfil its role as a contrast agent. In this context, macromolecular and supramolecular probes based on Gd complexes have been developed to improve the pharmacokinetic properties of these complexes, but also to improve the relaxivity values of existing contrast agents in order to increase contrast. One possible strategy is to increase the number of Gd per contrast agent by grafting several Gd complexes onto a peptide [70], thereby increasing the total relaxivity of the contrast agent. Another possible strategy for developing supramolecular MRI probes is the association of Gd complexes with peptides possessing self-assembly properties in nanostructures [11].

Developing MRI probes based on peptide self-assembly to increase the relaxivity of Gd complexes is very promising, but challenges still persist. Nanostructures as probes should allow improving relaxivity by increasing the rotational correlation time through an increase in molecular mass. The correlation time also depends on the flexibility of the Gd complex linked to the macromolecular or supramolecular structure. Studies have shown that a Gd complex linked to a nanostructure by a flexible spacer retains a fast rotational correlation time, with no significant difference from a simple Gd complex in solution [71]. Thus, the design of new MRI probes is still complex, as many parameters impact the correlation time. In addition, the complexation with contrast agents should not interfere with the self-assembling process and the interaction between possible targeting ligands and their receptors.

In this project, the P2-Gd(DOTAGA) was designed so as to provide the most efficient contrast agent. First, its sequence was optimized to enable specific functionalization by introducing a thiol group on which a Gd(DOTAGA) complex was conjugated to the peptide without flexible spacer. The presence of Gd(DOTAGA) could potentially encumber the RGD targeting motifs and prevent their interactions with $\alpha v \beta 3$ integrins. Therefore, mixtures of functionalized (P2-Gd(DOTAGA) and non-functionalized (P2) peptide at different molar ratio (i.e. 10, 15 or 20%),

were synthesized, with a view to their co-assembly. Such co-assembly would simultaneously expose the RGD motif and the Gd(DOTAGA) complex on the surface of the self-assembled nanoobject (Figure 7). The formulation of such co-assemblies was proved by the combined physicochemical characterizations, evidencing nanostructures with hydrodynamic diameters of 40 nm. Subsequently, MRI studies were performed to estimate and qualitatively compare their T1 and T2 imaging contrast and then quantitatively the relaxivity values of both monomers and co-assemblies at different ratios (P2-Gd(DOTAGA)10, P2-Gd(DOTAGA)15, P2-Gd(DOTAGA)20). The higher the relaxivity values, the more efficient the contrast agent is for MRI.

First, the relaxivity values of the P2-Gd(DOTAGA) conjugate mixtures in their monomeric form were measured, presenting well contrasting images, with a hypersignal in the T1 weighted image and a hyposignal in the T2 weighted image as expected for valuable MRI contrast agent. As a matter of comparison, Gd(DOTA) (Dotarem®), the clinical molecular Gd complex contrast agent providing the same elementary motif Gd(DOTA) used for the peptide functionalization was also analyzed (Figure 14).

P2-Gd(DOTAGA) presented r_2/r_1 values close to 1, similarly to Gd(DOTA) (Dotarem®). This indicates that the conjugate behaves like a T1 and T2 contrast agent. As for longitudinal relaxivities r_1, they increased by a factor of two, compared to Gd(DOTA). Since relaxivity is proportional to rotational correlation time (τ_R), this is congruent with the larger molecular weight of P2-Gd(DOTAGA) ($M = 1443.8$ g·mol^{-1}) compared to Gd(DOTA) ($M = 558.6$ g·mol^{-1}). These relaxivity results show the enhancement of the relaxivity of the Gd complexes when conjugated to the peptide, and a r_2/r_1 value at around 1, in accordance with characteristic values of T1 GBCAs. These initial results were encouraging for the next step towards self-assembly of peptide-based MRI agents (Table 3).

The formulation of the co-assembled P2 and P2-Gd(DOTAGA) mixtures were then analyzed by MRI at 7 T, providing qualitative T1 and T2 weighted images showing bright intensity in concentrated samples, and darker intensity, respectively. Considering the nanostructuration of the mixture with a significant increase in molecular weight, increases in r_1 and r_2 were expected as quantitative evaluation [72].
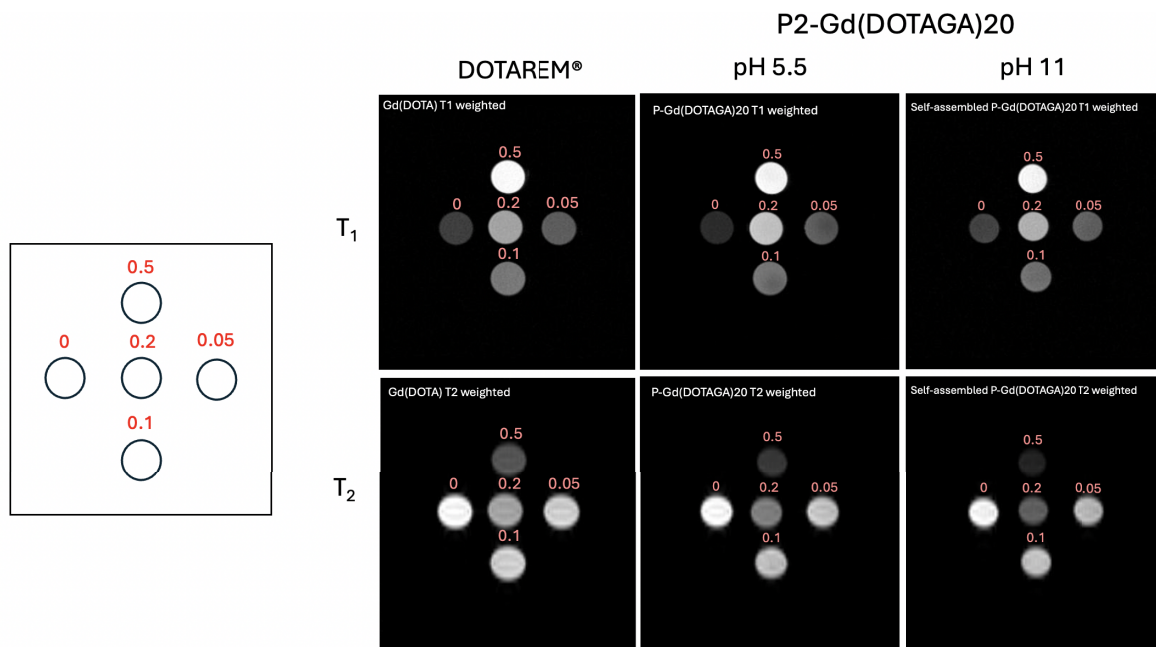
Figure 14. T1- and T2-weighted MRI images of Gd(DOTA) (DOTAREM®) and P2-Gd(DOTAGA)20 at pH 5.5 and pH 11, at 7 T, 293 K. Concentrations (red) are given in mM. Adapted from Ref. [47].

Table 3. Relaxivity values r_1, r_2 and r_2/r_1 of Gd(DOTA), and co-assembled P2-Gd(DOTAGA)x ($x + 10$, 15 or 20) at pH 5.5 and pH 11, at 7 T, 293 K

	r_1 (mM^{-1}·s^{-1})	r_2 (mM^{-1}·s^{-1})	r_2/r_1
Gd(DOTA) (Dotarem)	5.3	5.5	1.0
pH = 5.5			
P2-Gd(DOTAGA)10	13.6	14.5	1.1
P2-Gd(DOTAGA)15	12.1	14.2	1.2
P2-Gd(DOTAGA)20	11.0	14.0	1.3
pH = 11			
P2-Gd(DOTAGA)10	2.2	18.2	8.4
P2-Gd(DOTAGA)15	4.0	19.4	4.8
P2-Gd(DOTAGA)20	3.8	20.3	5.4

Standard deviation values is ±0.2 mM^{-1}·s^{-1}. Adapted from Ref. [47].

However, the results indicate a decrease in the r_1 value from monomeric to co-assembled form, in the range similar to that of Gd(DOTA). On the other hand, both r_2 and r_2/r_1 increased by a factor of 4 to 7. The notable increase in r_2/r_1 is typical of a nanoparticular relaxivity behavior [60] where the outer sphere contribution becomes predominant, due to magnetic susceptibility effects induced by high molecular weight scaffold of nanoparticle. The increase in r_2/r_1 value obtained for the co-assembled P2-Gd(DOTAGA) indicates a clear nanoparticular magnetic behavior.

The decrease in r_1 could be explained by the fact that relaxivity values not only depend on the rotational correlation time, but also on other factors such as the exchange rate of bulk water molecules with the Gd center [60]. As the Gd complex is not functionalized at the extreme end of the peptide, and is less accessible to water molecules in its nanoparticular form, the interaction with the water molecules could be reduced. Furthermore, the MRI analysis was performed in this study under a high field (7 T). Van Bochove et al. studied the impact of magnetic field intensity, either 1.41 T or 6.3 T, on the relaxivity values of a micelle made of Gd(DTPA)-bis(stearylamide) [73]. They determined a significant difference in r_1 values, i.e., $r_1 = 11.8$ mM^{-1}·s^{-1} and 4.5 mM^{-1}·s^{-1}, at 1.41 T and 6.3 T, respectively. Furthermore, they measured equivalent r_1 values as for the Gd(DTPA)-bis(stearylamide) monomer and an increased r_2 value of 13.0 mM^{-1}·s^{-1} at 6.3 T. Thus, the values obtained in this study are coherent with the literature. They confirm the co-assembly of the peptide-conjugate mixtures and are promising for the use of these nanostructurations for MRI imaging, when employing a lower magnetic field (1 T) for T1 contrast, but remain efficient at high magnetic field (7 T) for T2 contrast.

To enhance r_1 relaxivity, different improvements of the design of such contrast agents could be envisaged (1) by the use of a linker between the peptide and Gd(DOTAGA), or the conjugation of the complex at the extremity of the sequence, to make it more accessible to water molecules in bulk or, (2) the use of higher functionalization rates to generate higher P2-Gd(DOTAGA)/ P2 ratio, to increase the amount of Gd to the contrast agent. Nevertheless, these results are very promising for the development of self-assembled peptide-based MRI contrast agents, which could be exploited further for theranostic applications.

7. Conclusion

Peptide self-assembly nanostructures are promising biocompatible materials for theranostics. Their simultaneous use as intelligent systems for targeted and controlled drug delivery system and as an imaging probe for diagnostics is significant for the development of personalized medicine. However, many challenges remain in the design and characterization of such nanoobjects, and a deeper understanding of the interactions involved in self-assemblies is necessary for better control of their formation and further use for in vivo applications. Moreover, the functionalization of peptide sequences for theranostic applications needs to be optimized to maintain stable self-assembly and the desired imaging properties.

This synergistic multidisciplinary investigation enabled the development of syntheses and characterization methods that facilitate access to peptide sequences capable of self-assembling into nanostructures. The peptide sequences were designed to combine the expected properties for theranostic applications: (1) self-assembly for efficient drug encapsulation and biodistribution; (2) pH-sensitive self-assembly for drug delivery under a pH modification in the environment of cancer cells; (3) a receptor-targeting motif for specific and controlled delivery of the active ingredient to tumors; (4) accessible functions for further functionalization with a contrast agent for diagnosis. The simple, low time- and reactant-consuming protocol developed in flow chemistry and optimized with CE-ESI-MS, for sequence identification and purity, allowed to generate sequences that could be further used without any purification step. The efficient functionalization of these peptide sequences with an MRI probe optimized with CE-ESI-MS characterization allowed to generate mixtures of non-functionalized and functionalized peptides, that could be directly complexed with Gd(DOTAGA) and employed without purification for self-assembly or co-assembly formulations. Furthermore, a deep understanding of the mechanisms involved in peptide self-assembly could be obtained through the combination of analytical and physical methods, proving the obtention of physicochemical properties of interest in the fields of diagnostics and therapy. The physicochemical characterization of the self-assemblies or co-assemblies of the peptide mixtures proved the efficient formulation of stable nanorods, with rapid kinetics and dimensions of 30 nm length and 7 nm diameter, due to β-sheet interactions. The nanostructurations preserved the RGD motif on the surface for further efficient targeting and were demonstrated promising for MRI imaging when employing classical magnetic fields for medical diagnosis.

These results enrich the overall understanding of

such formulations of theranostic applications. Areas for improvement were identified by deep characterizations, that promote the design of new sequences in a rational and efficient way, to combine smart and targeted drug delivery and imaging properties for the nanostructures obtained from peptide building blocks formulation.

Declaration of interests

The authors do not work for, advise, own shares in, or receive funds from any organization that could benefit from this article, and have no affiliations other than their research organizations.

Acknowledgments

References

[1]   S. R. Tracey, P. Smyth, C. J. Barelle and C. J. Scott, *Biochem. Soc. Trans.* **49** (2021), pp. 2253–2269.

[2]   X. Shan, X. Gong, J. Li, J. Wen, Y. Li and Z. Zhang, *Acta Pharm. Sin. B* **12** (2022), pp. 3028–3048.

[3]   C. Zhang, L. Yan, X. Wang, S. Zhu, C. Chen, Z. Gu and Y. Zhao, *Nano Today* **35** (2020), article no. 101008.

[4]   M. S. Muthu, D. T. Leong, L. Mei and S.-S. Feng, *Theranostics* **4** (2014), pp. 660–677.

[5]   S. Mura and P. Couvreur, *Adv. Drug Deliv. Rev.* **64** (2012), pp. 1394–1416.

[6]   W. Poon, Y.-N. Zhang, B. Ouyang, B. R. Kingston, J. L. Y. Wu, S. Wilhelm and W. C. W. Chan, *ACS Nano* **13** (2019), pp. 5785–5798.

[7]   D. Tesauro, A. Accardo, C. Diaferia, V. Milano, J. Guillon, L. Ronga and F. Rossi, *Molecules* **24** (2019), article no. 351.

[8]   L. Lu, V. T. Duong, A. O. Shalash, M. Skwarczynski and I. Toth, *Vaccines* **9** (2021), article no. 563.

[9]   Z. Li, Y. Zhu and J. B. Matson, *ACS Appl. Bio Mater.* **5** (2022), pp. 4635–4651.

[10] J. Yang, H.-W. An and H. Wang, *ACS Appl. Bio Mater.* **4** (2021), pp. 24–46.

[11] C. Diaferia, E. Gianolio and A. Accardo, *J. Pept. Sci.* **25** (2019), article no. e3157.

[12] V. B. Kumar, B. Ozguney, A. Vlachou, Y. Chen, E. Gazit and P. Tamamis, *J. Phys. Chem. B* **127** (2023), pp. 1857–1871.

[13] Y. Wang, X. Zhang, K. Wan, N. Zhou, G. Wei and Z. Su, *J. Nanobiotechnol.* **19** (2021), article no. 253.

[14] I. Kim, S.-M. Jin, E. H. Han, E. Ko, M. Ahn, W.-Y. Bang, J.-K. Bang and E. Lee, *Biomacromolecules* **18** (2017), pp. 3600–3610.

[15] I. Kim, E. H. Han, J. Ryu, J.-Y. Min, H. Ahn, Y.-H. Chung and E. Lee, *Biomacromolecules* **17** (2016), pp. 3234–3243.

[16] C. Zhao, H. Chen, F. Wang and X. Zhang, *Colloids Surf. B: Biointerfaces* **208** (2021), article no. 112040.

[17] C. P. Gordon, *Org. Biomol. Chem.* **16** (2018), pp. 180–196.

[18] J. Liang, W.-L. Wu, X.-D. Xu, R.-X. Zhuo and X.-Z. Zhang, *Colloids Surf. B* **114** (2014), pp. 398–403.

[19] M. Ko, A. Quiñones-Hinojosa and R. Rao, *Cancer Metastasis Rev.* **39** (2020), pp. 519–534.

[20] F. Tagliaro, G. Manetto, F. Crivellente and F. P. Smith, *Forens. Sci. Int.* **92** (1998), pp. 75–88.

[21] Z. P. Gates and N. Hartrampf, *Pept. Sci.* **112** (2020), article no. e24198.

[22] I. M. Mándity, B. Olasz, S. B. Ötvös and F. Fülöp, *ChemSusChem* **7** (2014), pp. 3172–3176.

[23] E. Kaiser, R. L. Colescott, C. D. Bossinger and P. I. Cook, *Anal. Biochem.* **34** (1970), pp. 595–598.

[24] E. T. Sletten, M. Nuño, D. Guthrie and P. H. Seeberger, *Chem. Commun.* **55** (2019), pp. 14598–14601.

[25] A. J. Mijalis, D. A. Thomas, M. D. Simon, A. Adamo, R. Beaumont, K. F. Jensen and B. L. Pentelute, *Nat. Chem. Biol.* **13** (2017), pp. 464–466.

[26] C. Li, A. J. Callahan, K. S. Phadke, et al., *ACS Cent. Sci.* **8** (2022), pp. 205–213.

[27] C. Li, A. J. Callahan, M. D. Simon, et al., *Nat. Commun.* **12** (2021), article no. 4396.

[28] G. A. Acosta, M. del Fresno, M. Paradis-Bas, M. Rigau-DeLlobet, S. Côté, M. Royo and F. Albericio, *J. Pept. Sci.* **15** (2009), pp. 629–633.

[29] W. Wang, Y. Huang, J. Liu, et al., *Lab on a Chip* **11** (2011), pp. 929–935.

[30] A. Stolz, K. Jooß, O. Höcker, J. Römer, J. Schlecht and C. Neusüß, *Electrophoresis* **40** (2019), pp. 79–112.

[31] K. J. Rosnack, J. G. Stroh, D. H. Singleton, B. C. Guarino and G. C. Andrews, *J. Chromatogr. A* **675** (1994), pp. 219–225.

[32] C. Miller and J. Rivier, *J. Pept. Res.* **51** (1998), pp. 444–451.

[33] M. Hamdan, O. Curcuruto, S. Vigano and P. Rovero, *Rapid Commun. Mass Spectrom. RCM* **10** (1996), pp. 1128–1132.

[34] F. P. Gomes and J. R. Yates, *Mass Spectrom. Rev.* **38** (2019), pp. 445–460.

[35] J. Piestansky, P. Barath, P. Majerova, J. Galba, P. Mikus, B. Kovacech and A. Kovac, *J. Pharm. Biomed. Anal.* **189** (2020), article no. 113449.

[36] M. D. Cortez-Díaz, F. d'Orlyé, S. Gutierrez-Granados, L. M. de Leon-Rodriguez and A. Varenne, *Anal. Biochem.* **502** (2016), pp. 8–15.

[37] A. Am, M. E. Faccio, M. Pinvidic, et al., *J. Chromatogr. A* **1713** (2024), article no. 464496.

[38] S. Zhang, Z. Amso, L. M. De Leon Rodriguez, H. Kaur and M. A. Brimble, *J. Nat. Prod.* **79** (2016), pp. 1769–1774.

[39] P. W. R. Harris and M. A. Brimble, *Pept. Sci.* **100** (2013), pp. 356–365.

[40] E. I. Vrettos, N. Sayyad, E. M. Mavrogiannaki, et al., *RSC Adv.* **7** (2017), pp. 50519–50526.

[41] S. Fuse, Y. Otake and H. Nakamura, *Chem. – Asian J.* **13** (2018), pp. 3818–3832.

[42] Z. Zhou and Z.-R. Lu, *WIREs Nanomed. Nanobiotechnol.* **5** (2013), pp. 1–18.

[43] B. Todaro, E. Ottalagana, S. Luin and M. Santi, *Pharmaceutics* **15** (2023), article no. 1648.

[44] L. Carmès, M. Banerjee, P. Coliat, S. Harlepp, X. Pivot, O. Tillement, F. Lux and A. Detappe, *Adv. Ther.* **6** (2023), article no. 2300019.

[45] M. H. Stenzel, *ACS Macro Lett.* **2** (2013), pp. 14–18.

[46] J. M. J. M. Ravasco, H. Faustino, A. Trindade and P. M. P. Gois, *Chem. – Eur. J.* **25** (2019), pp. 43–59.

[47] A. Am, F. d'Orlyé, L. Trapiella-Alfonso, C. Lescot, B.-T. Doan and A. Varenne, *J. Chromatogr. A.* submitted.

[48] N. Brown, P. Rocchi, L. Carmès, et al., *Theranostics* **13** (2023), pp. 4711–4729.

[49] J. F. Desreux, E. Merciny and M. F. Loncin, *Inorg. Chem.* **20** (1981), pp. 987–991.

[50] G. Tircsó, E. Tircsóné Benyó, Z. Garda, et al., *J. Inorg. Biochem.* **206** (2020), article no. 111042.

[51] S. D. Fontaine, R. Reid, L. Robinson, G. W. Ashley and D. V. Santi, *Bioconjug. Chem.* **26** (2015), pp. 145–152.

[52] X. Yang, L. Ma, K. Lu and D. Zhao, *Protein J.* **43** (2024), pp. 464–476.

[53] R. Mu, D. Zhu, S. Abdulmalik, S. Wijekoon, G. Wei and S. G. Kumbar, *Bioact. Mater.* **35** (2024), pp. 181–207.

[54] A. Am, L. Trapiella Alfonso, C. Izabelle, B. Saubamea, B.-T. Doan, F. d'Orlyé and A. Varenne, *Anal. Bioanal. Chem.* (2024).

[55] J. S. Nowick, *Acc. Chem. Res.* **41** (2008), pp. 1319–1330.

[56] S. R. K. Ainavarapu, J. Brujić, H. H. Huang, et al., *Biophys. J.* **92** (2007), pp. 225–233.

[57] J. Wang, S. Han, G. Meng, H. Xu, D. Xia, X. Zhao, R. Schweins and J. R. Lu, *Soft Matter* **5** (2009), pp. 3870–3878.

[58] A. Hawe, W. L. Hulse, W. Jiskoot and R. T. Forbes, *Pharm. Res.* **28** (2011), pp. 2302–2310.

[59] Y.-D. Xiao, R. Paudel, J. Liu, C. Ma, Z.-S. Zhang and S.-K. Zhou, *Int. J. Mol. Med.* **38** (2016), pp. 1319–1326.

[60] A. S. Merbach, L. Helm and É. Tóth, *The Chemistry of Contrast Agents in Medical Magnetic Resonance Imaging* (A. Merbach, L. Helm and É. Tóth, eds.), John Wiley & Sons: New Jersey, 2013.

[61] S. Daksh, A. Kaul, S. Deep and A. Datta, *J. Inorg. Biochem.* **237** (2022), article no. 112018.

[62] S. Chen, L. An and S. Yang, *Molecules* **27** (2022), article no. 4573.

[63] C. Corot and D. Warlin, *Rev. Nanomed. Nanobiotechnol.* **5** (2013), pp. 411–422.

[64] G. W. Bourne and J. M. Trifaró, *Neuroscience* **7** (1982), pp. 1615–1622.

[65] J. Davies, P. Siebenhandl-Wolff, F. Tranquart, P. Jones and P. Evans, *Arch. Toxicol.* **96** (2022), pp. 403–429.

[66] A. Ghosh, M. Haverick, K. Stump, X. Yang, M. F. Tweedle and J. E. Goldberger, *J. Am. Chem. Soc.* **134** (2012), pp. 3647–3650.

[67] A. Koudrina and M. C. DeRosa, *ACS Omega* **5** (2020), pp. 22691–22701.

[68] L. Manzoni, L. Belvisi, D. Arosio, et al., *ChemMedChem* **7** (2012), pp. 1084–1093.

[69] L. Manzoni, L. Belvisi, D. Arosio, et al., *ChemMedChem* **4** (2009), pp. 615–632.

[70] P. Caravan, B. Das, S. Dumas, et al., *Angew. Chem. Int. Ed Engl.* **46** (2007), pp. 8171–8173.

[71] P. Caravan and Z. Zhang, *Eur. J. Inorg. Chem.* **2012** (2012), pp. 1916–1923.

[72] L. S. Arias, J. P. Pessan, A. P. M. Vieira, T. M. T. de Lima, A. C. B. Delbem and D. R. Monteiro, *Antibiotics* **7** (2018), article no. 46.

[73] S. Anjum, M. Hashim, S. A. Malik, M. Khan, J. M. Lorenzo, B. H. Abbasi and C. Hano, *Cancers* **13** (2021), article no. 4570.